

# STAVEBNÍ OBZOR

ČÍSLO 1/2016

Obsah čísla:

**LAMINAR SETTLING OF GLASS BEADS IN VISCO-PLASTIC LIQUIDS**

*Kesely Mikoláš, Matoušek Václav*

**DESIGN METHOD OF BENDING CAPACITY OF CONTINUOUS COMPOSITE SLAB**

*Liu Jin*

**A NOTE ON METHODS FOR THE ESTIMATION OF THE AIRBORNE SOUND INSULATION OF TIMBER FRAME STRUCTURES**

*Šlechta Jan*

**FLUCTUATION EFFECT OF EQUILIBRIUM MOISTURE CONTENT OF LOW SUBGRADE UNDER HIGH GROUNDWATER LEVEL IN HOT AND HUMID CLIMATIC REGIONS**

*Que Yun, Wu Jiabin*

**NUMERICAL MODEL APPLICATION IN ROWING SIMULATOR DESIGN**

*Chmátal Petr, Pollert Jaroslav and Švanda Ondřej*

# LAMINAR SETTLING OF GLASS BEADS IN VISCO-PLASTIC LIQUIDS

*Kesely Mikoláš<sup>1</sup>, Matoušek Václav<sup>1</sup>*

1. *Czech Technical University in Prague, Faculty of Civil Engineering, Department of Hydraulics and Hydrology, Prague, Thákurova 7, 166 29 Praha 6, Czech Republic; e-mail: mikolaskesely@seznam.cz*

## ABSTRACT

The paper deals with a determination of the terminal settling velocity of coarse particles in quiescent visco-plastic liquids of Herschel-Bulkley type. Experiments on laminar settling of glass beads of different sizes were conducted in transparent Carbopol solutions of various rheological properties in a sedimentation column. The terminal settling velocity of a solitude bead was determined together with the rheological parameters of the Carbopol liquid. An evaluation of the experimental results confirms the existence of the laminar regime for all tests and compares the measured velocities with predictions by Wilson et al. method. Furthermore, an alternative method is proposed for a prediction of the terminal settling velocity in the laminar regime which uses a particle-based determination of the strain rate in the expression for the equivalent viscosity. A comparison with our experimental results shows that the predictions using the proposed method agree well with the experiments and the proposed method is in the laminar settling regime more accurate than the Wilson et al. method.

## KEYWORDS

Non-Newtonian liquid, rheological properties, terminal settling velocity, equivalent viscosity

## INTRODUCTION

Many slurries of industrial interest are homogeneous mixtures of fine solid particles and water (or other liquid). If concentration of fines is high, then the mixtures exhibit a non-Newtonian behaviour. If coarse particles are present in the mixture as well (as for instance in mixtures of tailings and process water in mining operations), it is important to know whether the coarse particles are suspended in the non-Newtonian carrier, or they settle down. In slurry practice, a majority of non-Newtonian carriers are visco-plastic and hence exhibit a yield stress. If carrier liquid of this sort is subjected to acting of the shear stress, no strain rate is produced until the applied shear stress exceeds the yield stress. In case that a discrete particle is placed in a quiescent visco-plastic medium, the particle will not settle unless it is heavy enough to produce the shear stress sufficient to trigger particle settling. The fall of spherical particles in visco-plastic fluids was subject of numerous experimental studies over the last 50 years. Pioneer works built on methods for predicting the terminal settling velocity of spherical particles in Newtonian medium and modified Reynolds number or drag coefficient in order to use the methods for non-Newtonian fluids may be found, [1-2]. At the same time, an alternative approach was suggested to use graphs relating the drag coefficient with relevant dimensionless number based on rheological properties of the fluid, [3-4]. Later, detailed numerical simulations of the flow field surrounding a falling particle were published, [5-7]. Wilson et al.[8] proposed a direct (explicit) method for a prediction of the terminal settling velocity of spheres in both Newtonian and non-Newtonian liquids. Recently, Arabi and

Sanders [9] reported on their measurements of terminal settling velocities of metal spheres in clay-water suspensions with yield stress.

The aim of this paper is to collect own experimental results of terminal settling velocities of spherical glass beads in visco-plastic liquids in the laminar regime and to use them first to evaluate a predicting ability of the Wilson et al. [8] method and second to test an alternative method based on a different formulation of the equivalent viscosity required for settling velocity predictions.

## METHODS FOR PREDICTION OF TERMINAL SETTLING VELOCITY

### General equations

The terminal settling velocity of a spherical particle in quiescent fluid,  $V_{ts}$ , is expressed by using the following general equation, based on the balance of forces acting the settling particle,

$$V_{ts} = \sqrt{\frac{4(\rho_s - \rho_f)gd}{3\rho_f C_D}} \quad (1)$$

where  $\rho_s$  is the density of particle,  $\rho_f$  is the density of the fluid, and  $d$  is the diameter of a spherical particle. The equation (1) is valid for both Newtonian and non-Newtonian liquids. For the drag coefficient  $C_D$ , an analytical formula covering settling in a laminar regime is general too and it reads,

$$C_D = \frac{24}{Re_p} \quad (2)$$

In the drag-formula,  $C_D$  is related to the particle Reynolds number,

$$Re_p = \frac{\rho_f V_{ts} d}{\mu_{eq}} \quad (3)$$

which contains the equivalent (apparent, secant) viscosity,  $\mu_{eq}$ , representing rheology of the fluid. It is defined as

$$\mu_{eq} = \frac{\tau}{(du/dy)} \quad (4)$$

where  $\tau$  is the shear stress and  $du/dy$  is the strain rate. If the fluid is Newtonian, the equivalent viscosity is constant equal to the dynamic viscosity. If the fluid exhibits non-Newtonian behaviour, however,  $\mu_{eq}$  varies with the local shear rate associated with the particle settling. Moreover,  $\mu_{eq}$  needs to be related to other rheological parameters characteristic for particular non-Newtonian fluid. A solution of Equations 1-3 is iterative, which makes calculations of  $V_{ts}$  user-unfriendly.

In literature, efforts have been made to produce direct methods for the terminal settling velocity related to the Reynolds number.

### Wilson et al. method

The method by Wilson et al.[8] gives an explicit relationship between two dimensionless numbers to predict the terminal settling velocity of a spherical particle for all three regimes of settling (laminar, transitional, turbulent).

Based on an analogy of settling in Newtonian and non-Newtonian fluids, the method relates the dimensionless settling velocity  $V_{ts}/V'$  to the sphere shear Reynolds number  $Re^*$  defined as

$$\text{Re}^* = \frac{\rho_f V^* d}{\mu_{eq}} \quad (5)$$

where  $V^*$  is the mean shear velocity, which is defined using the mean surficial shear stress  $\bar{\tau}$  of a settling particle. This stress is expressed as the submerged weight divided by the surface area of the particle, which for a sphere is:

$$\bar{\tau} = \frac{(\rho_s - \rho_f)gd}{6} \quad (6)$$

As a result, the mean shear velocity is:

$$V^* = \sqrt{\frac{\bar{\tau}}{\rho_f}} = \sqrt{\frac{(\rho_s - \rho_f)gd}{6\rho_f}} \quad (7)$$

A relationship between  $V_{ts}/V^*$  and  $\text{Re}^*$  is calibrated so that it gives the same results as the indirect method by Turton and Levenspiel [10] for settling in Newtonian fluids. For the laminar regime ( $\text{Re}^* \leq 10$ ), the relationship is

$$\frac{V_{ts}}{V^*} = \frac{\text{Re}^*}{\left[3(1 + 0.08\text{Re}^{*1.2})\right]} + \frac{280}{\left[1 + 3 \cdot 10^4 \text{Re}^{*-3.2}\right]} \quad (8)$$

Wilson et al.[8] suggested to relate shear stress to the mean surficial shear stress at some reference level and to use a rheological model as an intermediary for a specification of a corresponding strain rate. If non-Newtonian fluid fits the Herschel-Bulkley rheological model, the equivalent viscosity is

$$\mu_{eq} = \frac{\tau_{ref}}{\left[(\tau_{ref} - \tau_y) / K\right]^{1/n}} \quad (9)$$

where  $\tau_y$ ,  $K$ ,  $n$  are rheological parameters of the Herschel-Bulkley model ( $\tau_y$  is the yield stress,  $K$  is the coefficient of consistency,  $n$  is the flow index). The reference shear stress,  $\tau_{ref} = \zeta \cdot \bar{\tau}$ , where the parameter  $\zeta = 0.3$  was based on authors' calibration using a set of 189 experimental data points. This solution means that the use of the method is limited to  $\tau_y < 0.3 \cdot \bar{\tau}$  as the value of equivalent viscosity would be less than 0 otherwise [9].

### Particle strain-rate based method

In the framework of the AMIRA P1087 project, V. Matoušek tested an alternative method for a determination of the equivalent viscosity at the shearing condition caused by particle settling. The method is based on a simple assumption that the strain rate for the rheological model of the fluid sheared by a settling particle is expressed as  $V_{ts}/d$ . Hence, for visco-plastic fluid which obeys the Herschel-Bulkley rheological model, the shear stress relevant to a spherical particle of the diameter  $d$  settling with the velocity  $V_{ts}$  is

$$\tau = \tau_y + K \left( \frac{du}{dy} \right)^n = \tau_y + K \left( \frac{V_{ts}}{d} \right)^n \quad (10)$$

The equivalent viscosity is according to Equation 4

$$\mu_{eq} = \frac{\tau_y + K(V_{ts}/d)^n}{V_{ts}/d} \quad (11)$$

This equivalent viscosity is used in Equations 1-3 to predict  $V_{ts}$ . This method is implicit.

## EXPERIMENTS

Experiments were carried out in the Water Engineering Laboratory of the Czech Technical University in Prague. Details of the experiments are given in the first-author's MSc thesis [11].

### Materials

As a non-Newtonian medium Carbopol (Ultrez 10) solutions were used. Carbopol is an acidic powder of particle size from 2 to 7 microns which, after dispersion in water and neutralization process, forms a non-Newtonian solution of Herschel-Bulkley type (rheology typical for thickened tailings). Values of the rheological parameters ( $\tau_y$ ,  $K$ ,  $n$ ) depend on a concentration of the powder in the solution. An advantage of Carbopol is its transparency and a quite simple preparation of solutions of various concentrations.

Coarse particles from four different fractions of narrow-graded glass beads were tested. The fraction TK2.0 with median size  $d_{50} = 2.01$  mm (particle sizes from 1.86 to 2.12 millimetres) and density  $\rho_s = 2426$  kg/m<sup>3</sup>. Slightly coarser fractions TK2.9 with particle sizes from 2.73 to 3.11 mm ( $d_{50} = 2.98$  mm,  $\rho_s = 2496$  kg/m<sup>3</sup>) and TK3.0 from 2.90 to 3.13 mm with  $d_{50} = 3.02$  mm and  $\rho_s = 2497$  kg/m<sup>3</sup>. The last fraction TK7.0 was narrow graded with all particle sizes finer than 7.65 mm and all particles coarser than 6.37 mm,  $d_{50} = 7.06$  and  $\rho_s = 2481$  kg/m<sup>3</sup>. All beads were considered spherical.

### Collected data set

In total, 33 experimental data points based on 124 measurements of  $V_{ts}$  in 10 Carbopol solutions of various rheological properties were collected (see Table 1).

Tab. 1: Experimental results

Test no.	$V_{ts}$ [cm/s]				Rheological parameters		
	TK2.0	TK2.9	TK3.0	TK7.0	$\tau_y$ [Pa]	$K$ [Pa.s <sup>n</sup> ]	$n$
1	0	0	0	2.40	2.27	1.43	0.53
2	0	0	0.02	2.42	2.25	1.34	0.54
3	0	0.02	0.07	4.31	2.07	1.07	0.55
4	0	0.13	0.09	6.25	1.64	0.87	0.57
5	0.01	0.18	0.23	8.93	1.29	1.04	0.54
6	0.02	0.25	0.30	10.65	1.26	0.94	0.55
7	0.04	0.28	0.33	9.74	1.39	1.19	0.53
8	0.11	0.51	0.60	12.50	0.77	0.84	0.55
9	0.15	0.77	0.83	14.35	0.63	0.71	0.57
10	0.51	2.12	2.08	199.01	0.33	0.55	0.58

### Test procedure

Terminal settling velocity was calculated by dividing the fixed vertical distance (333 mm) between two monitored planes in the sedimentation column with the measured time a particle needed to travel the distance between the two planes. At the top of the column the particle was carefully placed and released into the fluid paying attention not to induce any rotation or add initial force during the release. Each solid particle travelled a distance of 67 mm before reaching the first monitored plane. For every test series, at least 3 identical particles from each fraction were released into the sedimentation column and the average of measured velocities was reported as a single data point. Fluid samples were collected and rheological parameters measured in the rotational viscometer HAAKE VT 550 before and after the test series to ensure that the rheological properties of the fluid remained constant during the series.

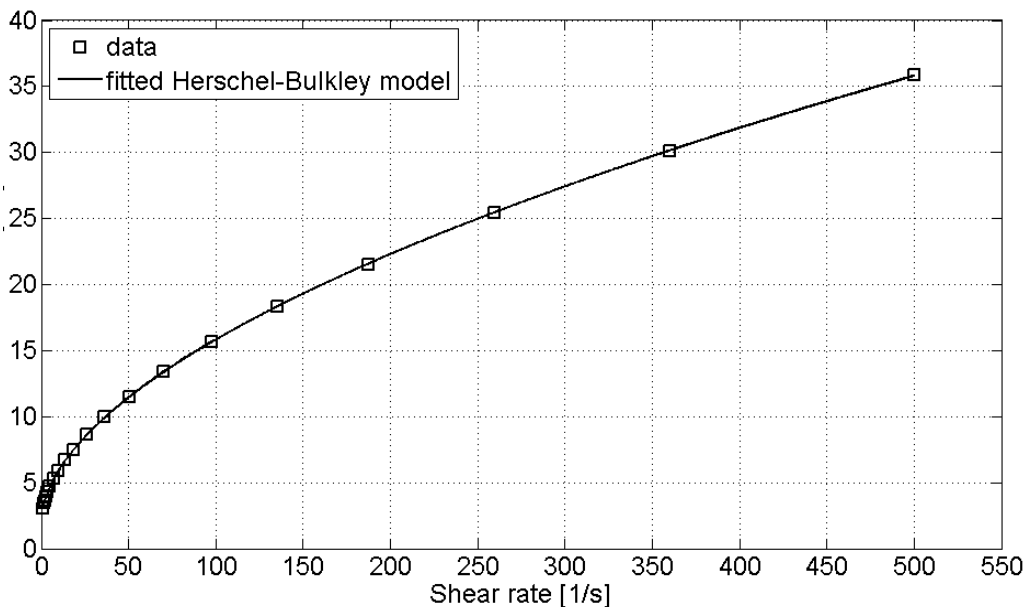


Fig. 1: Rheogram for Test series No. 3

### DISCUSSION OF RESULTS

The measured parameters ( $\tau_y$ ,  $K$ ,  $n$ ,  $d$ ,  $\rho_s$ ,  $V_{ts}$ ) are employed to evaluate an accuracy of the above described predictive methods for  $V_{ts}$ . In Figures 2 and 3, the results are presented in plots using the dimensionless groups proposed by Wilson et al.[8]. In Figure 2, the experimental results are compared to the predictions by the original Wilson et al.[8] method (Equations 5-9). Just 31 out of total 33 experimental data points could be used for the comparison due to the limitation of the method (it does not work at  $\tau_y \geq 0.3 \cdot \bar{\tau}$ ). Although some agreement is observed, the scatter is rather big. In Figure 3, the experimental results are compared to the predictions using the Wilson et al.[8] method (Equations 5-8) in which the particle strain-rate based method is used to calculate  $\mu_{eq}$  (Equation 11). This modified approach considerably improves the accuracy of the predictions (reduces the scatter). For  $Re^* < 1$ , the agreement between the measurements and predictions is excellent. At higher  $Re^*$  ( $1 < Re^* < 10$ ), the modified method tends to slightly underestimate values of  $V_{ts}$ .

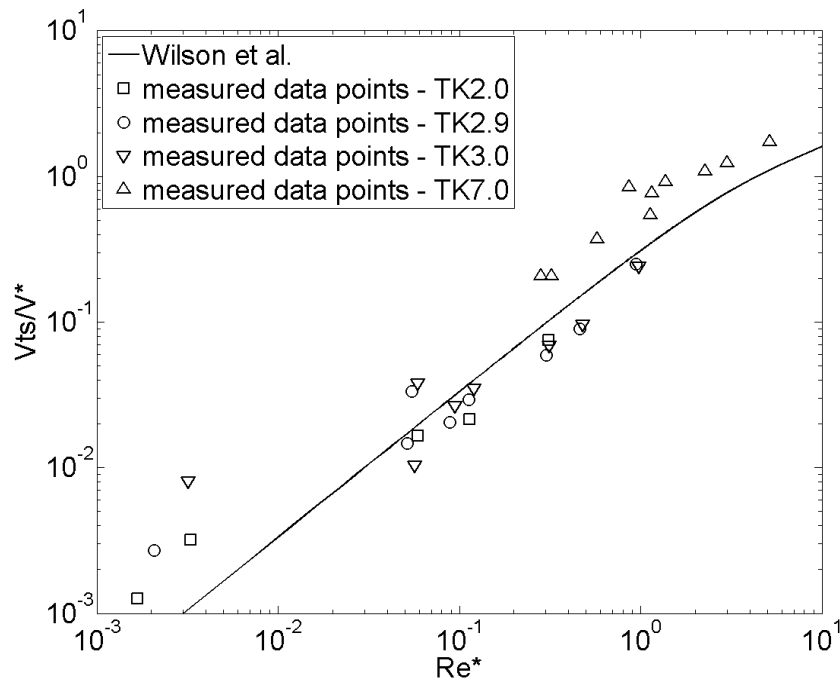


Fig. 2: Comparison of experimental data with Wilson et al.[8] technique

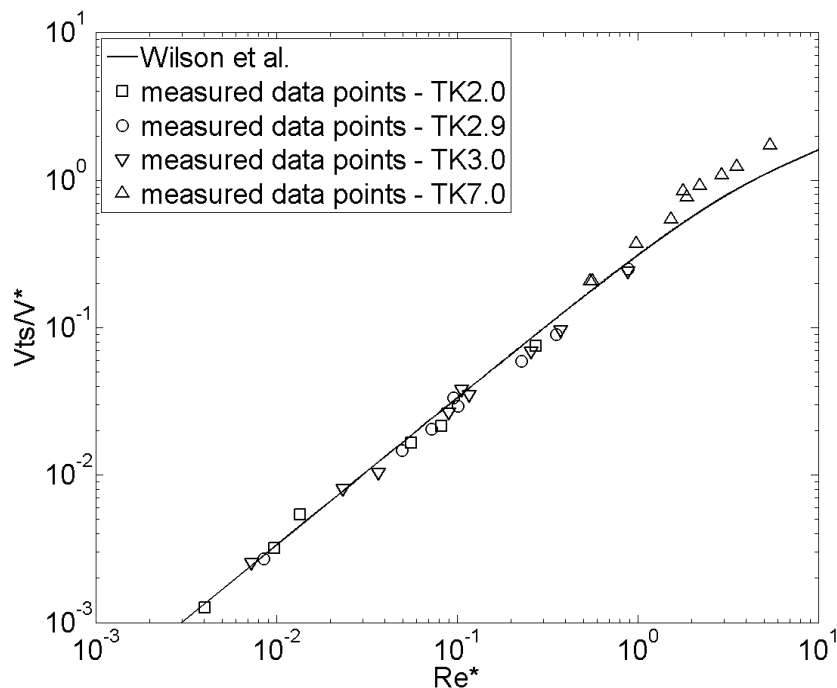


Fig. 3: Comparison of experimental data with particle strain-rate based method

Figure 4 compares experiments to predictions in the plot using the general equations (Equations 2-3). The plot confirms a validity of the Stokes law and hence the presence of the laminar regime in the entire range of measured settling conditions. This is consistent with our visual observations which did not recognize any wakes developed behind the settling particles.

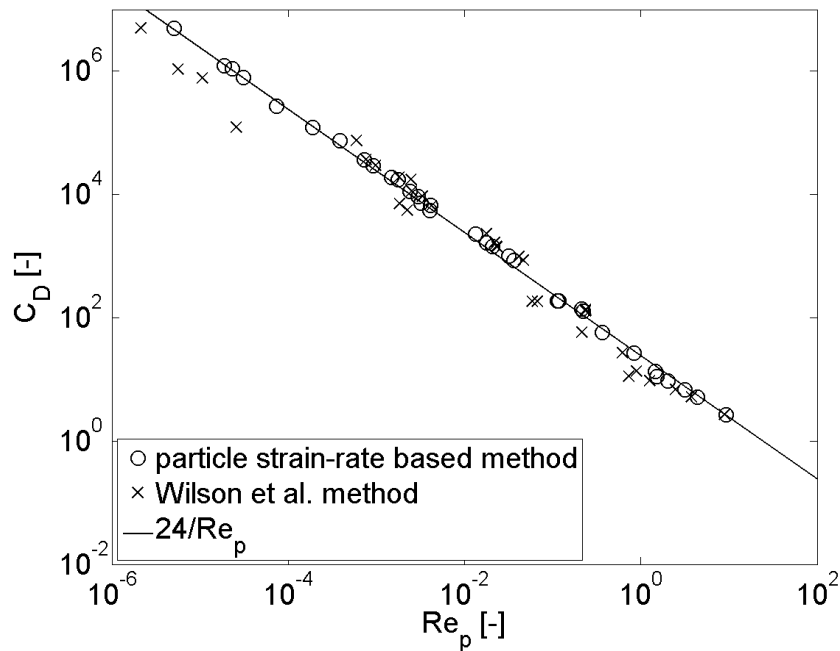


Fig. 4: Relation between drag coefficient  $C_D$  and particle Reynolds number  $Re_p$

The parity plot in Figure 5 shows that the deviation of the predicted  $V_{ts}$  from the measured  $V_{ts}$  is confined to  $\pm 30$  per cent if the particle strain-rate based method is used for the prediction. The deviation tends to be considerably bigger with the original Wilson et al.[8] technique used as a predictive method. The plot confirms that the proposed alternative method produces generally a better match.

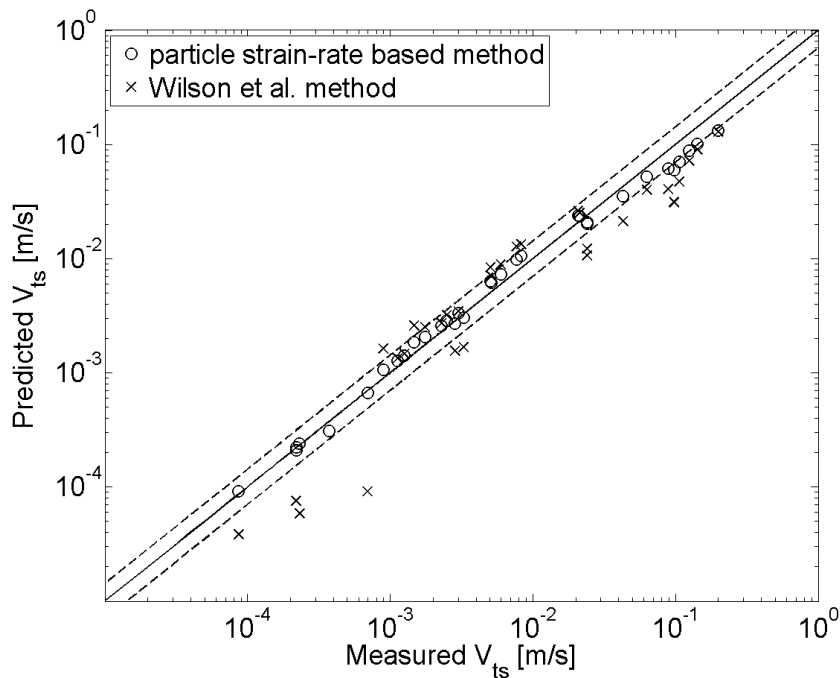


Fig. 5: Parity plot of measured and predicted terminal settling velocity. Legend: solid line = perfect match, dotted lines = +/- 30% deviation

## CONCLUSIONS

Our experimental investigation on laminar settling of glass beads in visco-plastic liquids reveals that the experimentally obtained terminal settling velocities can deviate from those predicted by the Wilson et al. [8] method with more than 30 per cent.

Overall accuracy of a prediction significantly improves in case that an alternative particle strain-rate based method is used for determining of the equivalent viscosity associated with shearing due to particle settling. On the other hand, the use of the particle strain-rate method makes the prediction of the terminal settling velocity an implicit procedure while the Wilson et al.[8] method is direct.

In the future work, the promising predictive ability of the particle-strain-rate-based method should be confirmed by comparing with a larger number of experimental data in the laminar regime. The method should be tested also in the transitional regime associated with higher values of particle Reynolds number.

## ACKNOWLEDGEMENTS

The experimental work was supported by the CTU project No. 8301300A001 carried out for CSIRO Australia in the framework of AMIRA P1087 project.

## REFERENCES

- [1] Valentik L., Whitmore R. L., 1965. Terminal Velocity of Spheres in Bingham Plastics. *British Journal of Applied Physics*, vol. 16: 1197-1203
- [2] Ansley R.W., Smith T.N., 1967. Motion of Spherical Particles in a Bingham Plastic. *American Institute of Chemical Engineers*, vol. 13: 1193-1196
- [3] Anders U.Ts., 1961. Equilibrium and Motion of Spheres in a Viscoplastic Liquid. *Soviet Physics-Doklady*, vol. 5: 723
- [4] du Plessis M.P., Ansley R.W., 1967. Settling Parameters In Solid Pipelining. *Journal of the Pipeline Division (American Society of Civil Engineers)*, vol. 93: 1
- [5] Beris A.N., Tsamopoulos J., Armstrong, R.C., Brown, R.A., 1985. Creeping Motion of a Sphere Through a Bingham Plastic. *Journal of Fluid Mechanics*, vol. 158: 44-219
- [6] Blackery J., Mitsoulis, E., 1997. Creeping Motion of a Sphere in Tubes Filled with a Bingham Plastic Material, *Journal of Non-Newtonian Fluid Mechanics*, vol. 70: 59-77
- [7] Beaulne M., Mitsoulis E., 1997. Creeping Motion of a Sphere in Tubes Filled with Herschel-Bulkley Fluids. *Journal of Non-Newtonian Fluid Mechanics*, vol. 72: 55
- [8] Wilson K.C., Horsley R.R., Kealy T., Reizes J.A., Horsley M., 2003. Direct Prediction of Fall Velocities in Non-Newtonian Materials. *International Journal of Mineral Processing*, vol. 71: 17-30
- [9] Arabi A.S., Sanders R.S., 2014. Particle terminal settling velocities in non-Newtonian, viscoplastic fluids. In: *Hydrotransport 19*, edited by VirtualPiE Ltd t/aBHR Group, 449-458



- [10] Turton R., Levenspiel O., 1986. A Short Note on Drag Correlation for Spheres. Powder Technology, vol. 47: 83
- [11] Kesely M., 2016. Evaluation of Settling Velocity of Coarse Particles in Visco-plastic Fluid and Frictional Loss in Complex Slurry Flow (MSc thesis at Czech Technical University in Prague) 51 pp.

# DESIGN METHOD OF BENDING CAPACITY OF CONTINUOUS COMPOSITE SLAB

Liu Jin<sup>1</sup>

1. Faculty of architecture and urban planning, Chongqing, 400045, China;  
e-mail: lj68832533@163.com

## ABSTRACT

This paper presents a calculation method for predicting the ultimate loading capacity of continuous composite slabs. Only the small scale slide block test was needed to determine few mechanical parameters, and less cost had to be paid, in comparison to the conventional m-k method. Various load conditions and parameters were considered. Comparisons between test results and predicted results have shown that the proposed method has enough precision. Furthermore, the simplified method was also proposed for practical design.

## KEYWORDS

profiled steel sheet; simplified design; bending capacity

## 1. INTRODUCTION

Composite slabs with profiled steel sheet have been widely used in practical structures since the 60's of the last century. In practice, compared with conventional reinforced concrete slabs, composite slabs have major advantages: no formworks and fewer scaffolds, higher loading capacity, lighter weight and faster construction speed. Furthermore, due to the composite action created by the bond and mechanical occlusion on the interface between the concrete and profiled steel sheet, the material strength of composite slabs can be fully utilized.

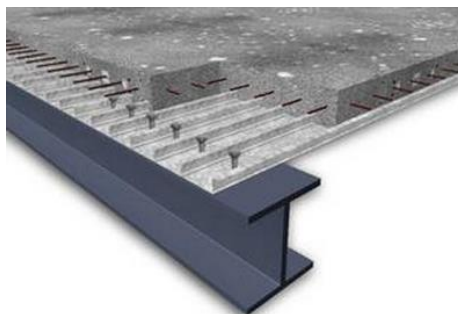


Fig. 1: Continuous composite floor with profiled steel sheet

Nowadays, there are many studies available about the simply supported composite slabs with single span [1 - 5], including experimental studies, theoretical models and design methods. However, as shown in Fig.1, continuous slabs often exist in practical structures, and some tests have been already carried out [6, 7], showing that the loading capacity of continuous composite slabs was much higher than that of simply supported slabs. Then the regression method, called m-k method, has been used for calculating the ultimate loading capacity of continuous composite slabs. In order to apply the m-k method shown in Fig.2, a large number of tests on full-scale slab specimens must be carried out by changing the geometrical dimensions and material strength

levels and to determine the relation between the ultimate loading capacity versus various geometrical and material parameters of continuous composite slabs. Therefore, the high cost must be paid for obtaining the regression equation of composite slabs with various types of profiled steel sheet.

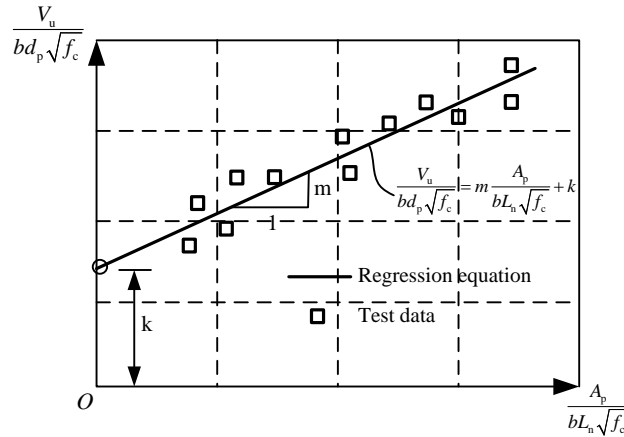


Fig. 2: *m-k method for determining ultimate loading capacity of composite slabs*

As shown in Fig.3, there are mainly four failure modes of composite slabs with profiled steel sheet [8]: (1) Flexure failure: at mid-span, the section of the profile steel sheet yield, and then the concrete crush, but the longitudinal interface between the steel sheet and concrete keeps good condition and little slip can be observed nearing the support. (2) Longitudinal shear failure: large slip exists on the interface, but the section at mid-span does not yield. (3) Vertical shear failure: when the ratio of the span to the height of the slab is relative small, the diagonal crack will appear near the support, similar to the shear failure mode of conventional reinforced concrete slabs. (4) Punching shear failure: when the thin slab bears heavy concentrated load, the cone shaped cracking occurs near the load point.

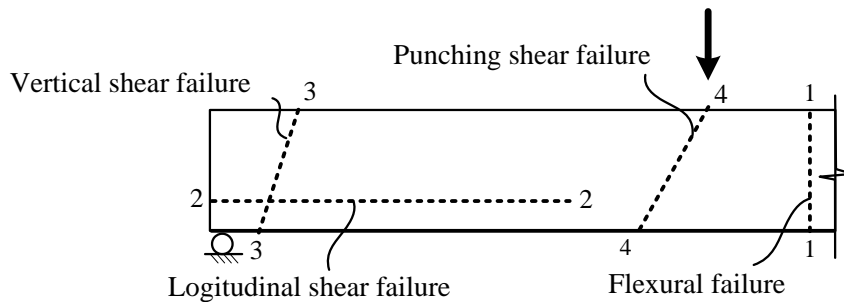


Fig. 3: *Failure modes of composite slab*

From the test results available now, it can be found that the flexure failure and longitudinal shear failure were the most common failure modes of composite slabs with steel sheet. Johnson has proposed simplified equations for calculating the ultimate capacity of composite slabs with vertical shear failure and punching shear failure modes [9], and the flexural capacity of the continuous composite slab can be directly obtained by the plastic equilibrium conditions on the section. Therefore, the method for calculating the longitudinal shear capacity of the continuous composite slab needed to be studied.

In this paper, a new theoretical model was developed for predicting the ultimate loading capacity of continuous composite slabs with profiled steel sheet, and the test validation was also made, in order to investigate the precision of the theoretical model. Finally, the simplified design

methods were proposed for calculating the ultimate loading capacity of continuous composite slabs with profiled steel sheet in practice.

## 2. THEORETICAL MODEL

Firstly, in order to simplify the expression formulas in theoretical derivation, the section of the profiled steel sheet was equivalent to an I-shape section. As shown in Fig.4, the width and the thickness of the flange and the height of the web plate of the I-shape section were equal to the section of the profiled steel sheet, and the thickness of the web plate  $t_w=2t/\cos\alpha$ , where  $t$  was the thickness of the profiled steel sheet, and  $\alpha$  was the inclining angle of the web of the profiled steel sheet.

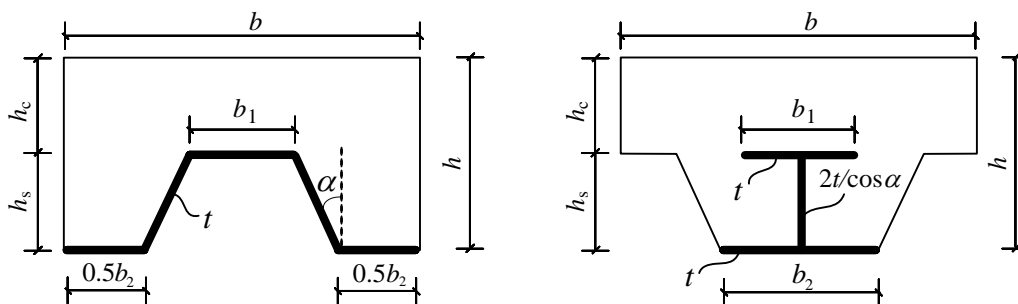


Fig. 4: Simplification for composite section

### 2.1 $M_u$ - $T_u$ relation

As illustrated in Fig.5, at ultimate state, the relation between the ultimate flexural capacity  $M_u$  of the section and the tensile force  $T_u$  of the profiled steel sheet could be determined by the slip strain  $\epsilon_r$  on the interface. The  $M_u$  versus  $T_u$  relation had been assumed to be linear by Patrick [10]. However, the conclusions in the reference [3] indicated that the linear assumption of the  $M_u$  versus  $T_u$  relation would underestimate the longitudinal shear capacity of composite slabs with profiled steel sheet. Therefore, the  $M_u$  versus  $T_u$  relation should be discussed in detail.

Fig.5 showed three typical strain and stress distribution state of the composite section, corresponding to different shear connection degrees. When there was no composite action on the interface (Fig.5a), the concrete and steel sheet resisted the bending moment alone, and no axial force existed on the pure concrete section and the pure steel sheet section. If the concrete and steel sheet were completely composed (Fig.5c), there would be no slip on the interface, so the ultimate flexure loading capacity could be achieved. However, as shown in Fig.5b, in general, the slip often existed between the steel sheet and concrete, especially for slabs with longitudinal failure modes, so the theoretical model for calculating the ultimate loading capacity of continuous composite slabs should be established.

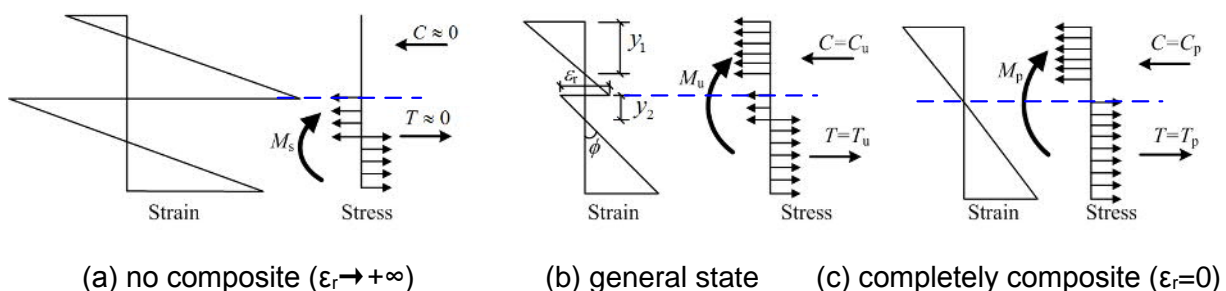


Fig. 5: Strain and stress distribution on section (sagging moment and full plasticity state)

According to the axial force equilibrium condition on the section, the equation could be obtained as:

$$f_y t_w (h_s - 2t - y_2) + f_y b_2 t = f_c b y_1 + \int_0^{y_1} f_c b(y) dy + f_y b_1 t + f_y t_w (y_2 - t) \quad (1)$$

where  $f_y$  was the yield strength of the steel and  $f_c$  was the compressive strength of the concrete.  $y_1$  and  $y_2$  were the height of the compressive zone of concrete and steel sheet respectively.  $b(y)$  was the width of the concrete section below the top flange of the steel sheet.

Then the equations for calculating  $M_u$  and  $T_u$  could be expressed as:

$$\begin{cases} M_u = f_y b_2 t h + f_y t_w (h_s - y_2)(h_c + 0.5h_s + 0.5y_2) - 0.5f_c b y_1^2 \\ \quad - f_y b_1 t h_c - f_y t_w y_2 (h_c + 0.5y_2) - \int_0^{y_1} f_c b(y)(h_c + y) dy \\ T_u = f_y t_w (h_s - 2y_2) + f_y (b_2 - b_1) t \end{cases} \quad (2)$$

Introducing equation (1) into equation (2), the parametric equation group about  $M_u$  and  $T_u$  with single parameter  $y_2$  could be obtained. It could be observed that the tensile force  $T_u$  of the profiled steel sheet had a linear relation with  $y_2$  and the ultimate flexural capacity  $M_u$  of the section had a parabolic relation with  $y_2$ , so there was parabolic relation between  $M_u$  and  $T_u$ , which was plotted in Fig.6.

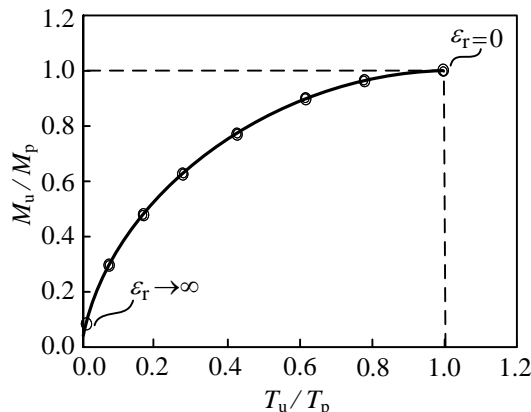


Fig. 6: Relation between  $M_u$  and  $T_u$

As shown in Fig.5, there were totally two mechanical boundary conditions:

(1) when the slip strain  $\epsilon_r$  equalled to zero, the tensile force  $T_u$  of the profiled steel sheet was equivalent to its upper limit  $T_p$ , and the ultimate flexural capacity  $M_u$  of the section was equivalent to its upper limit  $M_p$ .

(2) when there was no bond between the profiled steel sheet and concrete ( $\epsilon_r$  approaching infinite), the profile steel sheet was at pure bending state, so the tensile force  $T_u$  of the profiled steel sheet was equivalent to zero, and  $M_u = M_s$ , where  $M_s$  was the flexural capacity of the pure section of the profiled steel sheet.

Based on a large number of numerical calculations, the  $M_u$  versus  $T_u$  relation could be obtained, as shown in Fig.6. Furthermore, the  $M_u$  versus  $T_u$  relation could be simply expressed as:

$$\frac{M_u}{M_p} = 1 - \left(1 - \frac{M_s}{M_p}\right) \left(\frac{T_u}{T_p} - 1\right)^2 \quad (3)$$

where the equations for calculating  $M_s$  and  $M_p$  could be expressed as:

$$M_s = f_y W_p \tag{4}$$

$$M_p = f_y A_p (h - e_p - 0.5 f_y A_p / f_c b) \tag{5}$$

where  $W_p$  and  $A_p$  were the plastic moment and the section area of the profiled steel sheet,  $e_p$  was the distance from the bottom of the slab to the plastic neutral axis of the profiled steel sheet.

After the  $M_u$  versus  $T_u$  relation was obtained, the ultimate tensile force  $T_u$  of the profiled steel sheet section should be determined. In continuous slabs, as shown in Fig.7, the longitudinal shear failure surface might appear in two segments along the span: the segment A between the inflection point of the bending moment diagram and the load point, and the segment B between the side bearing and the load point. According to the force equilibrium condition, the ultimate tensile force  $T_u$  of the profiled steel sheet section was equivalent to the longitudinal shear force on the interface between the profiled steel sheet and concrete.

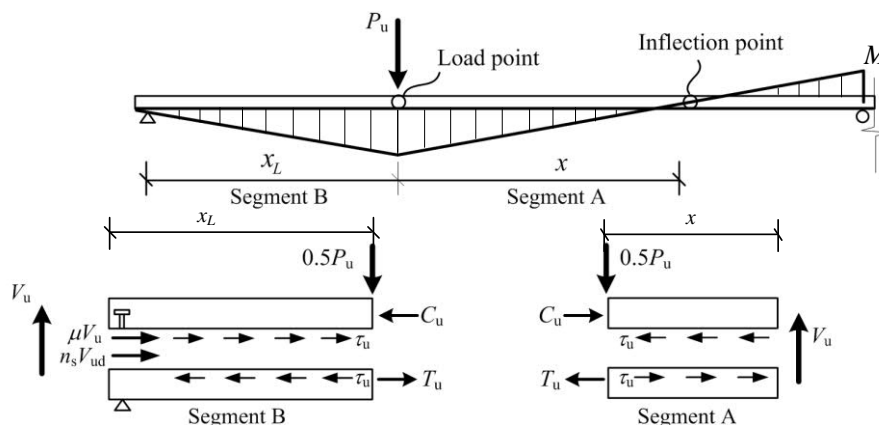


Fig. 7: Mechanical state of continuous composite slab at ultimate state

As shown in Fig.7, when the longitudinal interface of the segment A failed, the ultimate tensile force  $T_u$  of the section of the profiled steel sheet could be calculated as:

$$T_{u,A} = \tau_u b x \leq T_p = f_y A_p \tag{6}$$

where  $\tau_u$  was the shear strength of the interface between the profiled steel sheet and concrete, which could be calculated as<sup>[10]</sup>:

$$\tau_u = \nu \sqrt{f_c'} \tag{7}$$

where  $f_c'$  was the cylinder compressive strength of the concrete.  $\nu$  was the bond coefficient of the interface determined by the types and constructions of the profiled steel sheet, which could be obtained by the small scale slide block tests with low cost and high precision (Fig.8).

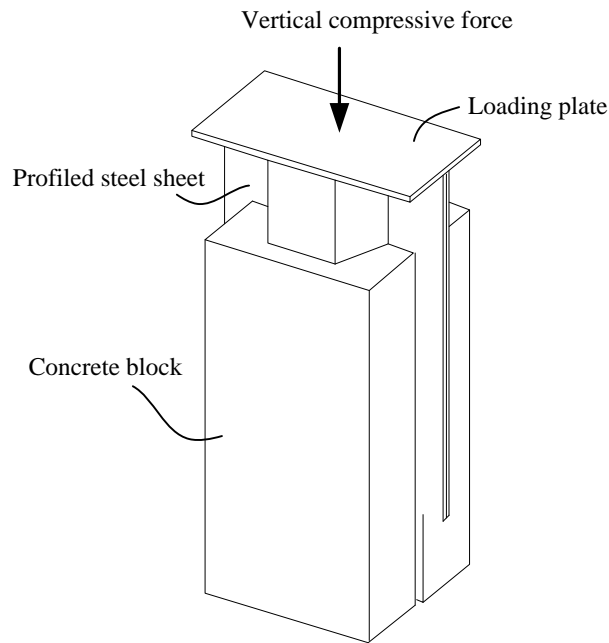


Fig. 8: Slide block test for determining bond coefficient between the steel sheet and concrete

As shown in Fig.7, when the longitudinal interface of the segment B failed, the ultimate tensile force  $T_u$  of the section of the profiled steel sheet could be regarded as the summation of three parts: (1) the shear stress on the interface, (2) the frictional force produced by the reaction force of the side bearing, (3) the shear capacity of studs at the edge. Therefore, the ultimate tensile force  $T_u$  of the section of the profiled steel sheet determined from the segment B could be obtained as:

$$T_{u,B} = \tau_u b x_L + \mu V_u + n_s V_{ud} \leq f_y A_p \quad (8)$$

where  $\mu$  was the frictional coefficient between the profiled steel sheet and concrete, which could be also determined by small scale slide block tests.  $V_u$  was the ultimate vertical shear force near the side bearing,  $n_s$  was the number of studs at the edge, and  $V_{ud}$  was the shear capacity of the stud, which could be calculated as<sup>[11]</sup>:

$$V_{ud} = 0.43 A_{st} \sqrt{E_c f_c} \leq 0.7 f_u A_{st} \quad (9)$$

where  $A_{st}$  was the section area of the stud,  $f_u$  was the tensile strength of the stud, and  $E_c$  was the elastic modulus of the concrete.

Finally, the ultimate tensile force  $T_u$  of the profiled steel sheet section could be determined as:

$$T_u = \min (T_{u,A}, T_{u,B}) \quad (10)$$

## 2.2 Ultimate loading capacity of continuous slab

Based on the  $M_u$  versus  $T_u$  relation of the composite section and the force equilibrium condition along the span, the ultimate loading capacity of the continuous composite slab could be calculated. Firstly, in order to obtain the area of the longitudinal shear failure surface, the position of the inflection point of the bending moment diagram should be determined, but it was related to the ultimate positive bending moment at the load point. Therefore, the iterative solution needed to

be carried out. In the following parts, the methods for calculating the ultimate loading capacity of continuous composite slab under various load condition were discussed in detail.

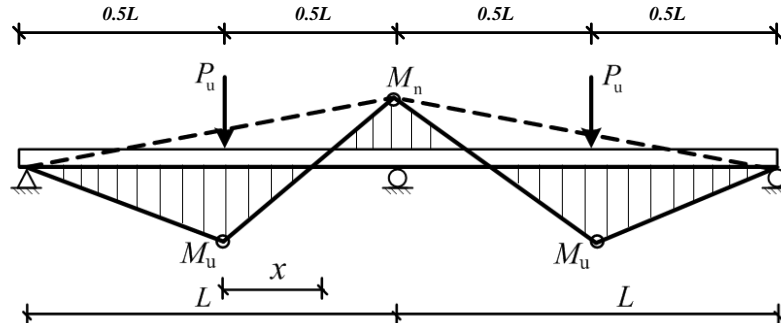


Fig. 9: Bending moment diagram of two-span continuous slab subjected to single point load

As shown in Fig.9, for the two-span continuous slab subjected to single concentrated load at mid-span of each span, according to the force equilibrium condition, the bending moment  $M_u$  at the load point could be calculated as:

$$M_u = 0.25P_uL - 0.5M_n \tag{11}$$

where  $M_n$  was the ultimate negative capacity of the composite section at the mid bearing.

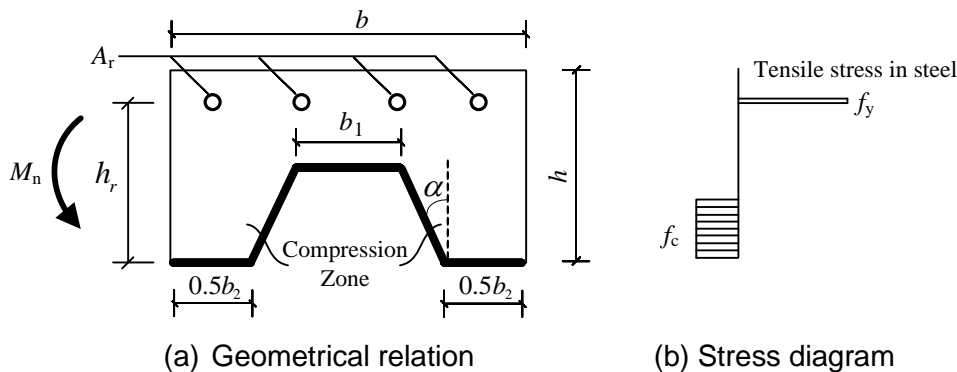


Fig. 10: Calculation model for negative moment

The existing test results indicated that the local buckling of the profiled steel sheet always occurred when the section of the composite slab subjected to negative bending moment, so the contribution of the profiled steel sheet to the negative ultimate capacity  $M_n$  of the composite section must be neglected. As shown in Fig.10, the negative ultimate capacity  $M_n$  of the composite section could be calculated as:

$$M_n = f_{yr}A_r(h_r - 0.5f_{yr}A_r / f_c b) \tag{12}$$

Where  $A_r$  and  $f_{yr}$  were the total area and yielding strength of the steel bars at the top of the section,  $h_r$  was the distance from the steel bars to the bottom of the composite section.

Based on the bending moment diagram shown in Fig.9, the position of the inflection point could be determined as:

$$x = 0.5L \frac{M_u}{M_u + M_n} \tag{13}$$

Taking equation (3), (6), (11), (12) and (13) as a non-linear equation group, the ultimate loading capacity of the continuous composite slab could be obtained by the iterative solution

method, which was illustrated in Fig.11.  $\Delta M$  was the incremental moment at each iterative step, which could be determined according to the solution precision, and  $e$  was the error limit for the iterative solution.

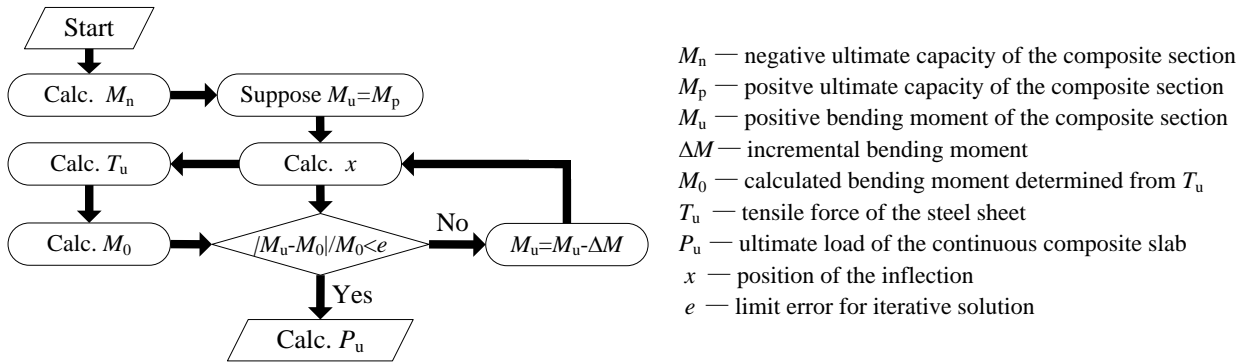


Fig. 11: Iterative flow for solving non-linear equation group

### 3. TEST VERIFICATION

In order to verify the proposed theoretical model, the comparative calculations were made based on tests in references [12] and [13]. The detailed results were illustrated in Table 1. It could be observed that the proposed method has enough precision for predicting the ultimate loading capacity of continuous composite slab with steel sheet.

Tab. 1: Comparative results between the predicted results and the test results

Ref No.	Specimen No.	L/mm	h/mm	$P_{u, cal} / kN$	$P_{u, test} / kN$	$P_{u, cal} / P_{u, test}$
Chen [12]	B-6	2600	165	138.33	146.80	0.94
	B-7a	2600	165	140.25	119.75	1.17
	B-7b	3200	165	106.58	119.75	0.89
Lee [13]	CSI-130-0.4(HS)	3000	130	91.57	96.00	0.95
	CSI-150-0.4(HS)	3000	150	110.81	110.00	1.00
	CSI-150-0.4(MS)	3000	150	111.42	128.00	0.87

### 4. CONCLUSION

Comparison with the test results showed that the theoretical method had enough precision for predicting the ultimate loading capacity of continuous composite slabs. Different from conventional m-k method with high cost, only the small scale slide block test with low cost had to be carried out to find the bond coefficient.

The simplified method could be used for continuous composite slabs subjected to the uniform distributed load in practical design, and the flexural failure mode and longitudinal shear failure mode were both considered.

## REFERENCES

- [1] Zona A., Barbato M. and Conte J. P. Nonlinear seismic response analysis of steel–concrete composite frames. *Journal of Structural Engineering*, 2008, 134(6): 986-997
- [2] E. Spacone and El-Tawil S. Nonlinear analysis of steel-concrete composite structures: state of the art. *Journal of Structural Engineering*, 2004, 130(2): 159-168
- [3] Crisinel M. and Marimon F. A new simplified method for the design of composite slabs. *Journal of Constructional Steel Research*, 2004, 60: 481-491
- [4] Vainiunas P, Valivonis J, Marciukaitis G, et al. Analysis of longitudinal shear behavior for composite steel and concrete slabs. *Journal of Constructional Steel Research*, 2006, 62:1264–1269
- [5] Wright H D, Evans H R, Harding P W. The use of profiled steel sheeting in floor construction. *J. Construct. Steel Research*, 1987, 7:279–295
- [6] Porter M L, Ekberg C E. Behavior of steel-deck-reinforced slabs. *ASCE-Journal of Structural Engineering*, 1977, 103 (3): 663~667.
- [7] Daniels B J, Crisinel M. Composite slab behavior and strength analysis. part 2:comparisons with test results and parametric analysis. *ASCE-Journal of Structural Engineering*, 1993 , 119 (1) :36-49.
- [8] Schuster R M. Composite steel-deck concrete floor systems. *Journal of the Structural Division*, 1976, 5: 899–917
- [9] Johnson R P. *Composite Structures of Steel and Concrete, Volume 1, Beams, Slabs, Columns and Frames for Buildings*. Oxford: Blackwell Scientific Publication, 1994.
- [10] Patrick M. A new partial shear connection strength model for composite slabs. *Journal of the Australian Institute of Steel Construction*, 1990, 24(3):2–16.
- [11] Nie J G, Cai C S, Steel-concrete composite beams considering shear slip effects, *ASCE-Journal of Structural Engineering*, 2003, 129(4): 495-506.
- [12] Chen S M. Study of load carrying capacities of 3W DECK composite slabs. *Journal of Building Structures*, 2002, 23(3):19–26.
- [13] Lee L, Quek S, Ang K. Moment redistribution in continuous profiled steel-concrete composite slabs. *Magazine of Concrete Research*, 2001, 53(5):301–309.

# A NOTE ON METHODS FOR THE ESTIMATION OF THE AIRBORNE SOUND INSULATION OF TIMBER FRAME STRUCTURES

Jan Šlechta<sup>1</sup>

1. *Czech Technical University in Prague, University Centre for Energy Efficient Buildings, Buštěhrad, Třinecká 1024, 273 43, Czech Republic; jan.slechta@cvut.cz*

## ABSTRACT

Acoustic behavior of structures with wooden elements is nowadays of great interest. At the same time, the estimation of the airborne sound insulation of timber frame structures is a complex procedure which includes the prediction of several resonances and the analysis of a significant decrease of the transmission loss in the low frequency range.

Three case studies are presented in the paper. The emphasis is put on the transmission loss in 1/3 octave frequency bands of double leaf structures with gypsum panels, wood studs and a well-damped cavity. Methods of Sharp and Davy are used for the transmission loss prediction. Particular issues are discussed for an asymmetrically sheathed timber frame structure, wood studs with resilient channels and staggered studs.

The paper also presents that the weighted sound reduction index is not sufficient quantity for characterizing the airborne sound insulation of timber frame structures. Various methods are employed for the calculation of the transmission loss of a traditional structure on a silicate base. Characteristic differences between a silicate based structure and a timber frame structure are highlighted. The usage of the spectrum adaptation terms is encouraged.

The paper intends to be helpful in the field of the transmission loss estimation of double leaf structures with wood studs. Since the acoustic behavior of double leaf structures with wood studs is certainly a complex phenomenon, there is a further need for an improvement of methods for the transmission loss estimation and single number quantities for the evaluation of the sound insulation.

## KEYWORDS

Sound insulation; timber frame structures; transmission loss; weighted sound reduction index; resonance frequency

## INTRODUCTION

A trend of contemporary society is to increase the living standard constantly together with an effort to achieve the sustainable construction. Timber frame houses belong among structures which are considered to be environmentally friendly and at the same time energy (and therefore also financially) efficient. Nevertheless, one should not neglect the importance of the acoustic comfort when designing houses with wooden elements.

Since timber frame houses are lightweight and double leaf structures, their acoustic behavior differs significantly from the acoustic behavior of widely used heavy-weight materials as bricks or concrete. The airborne sound insulation is usually characterized by the sound reduction

index (abbrev. SRI) in 1/3 octave frequency bands. The term transmission loss (abbrev. TL) is interchangeable with the term SRI in this paper.

The evaluation of the TL in 1/3 octave frequency bands is too complex for practical use and there is need for single number quantities for the assessment of the sound insulation. Vast investigation made by COST Action TU0901 [1] revealed that 16 European countries (out of 30) are applying only the weighted apparent sound reduction index  $R'_w$  for evaluating the airborne sound insulation.  $R'_w$  is calculated for center frequencies of 1/3 octave bands ranging from 100 Hz to 3150 Hz according to the standard ISO 717-1 [2].

ISO 717-1 also describes the spectrum adaptation terms  $C$  and  $C_{tr}$  both for the standard frequency spectrum (from 100 Hz to 3150 Hz) and for the extended frequency spectrum (from 50 Hz to 5000 Hz). Only one country (Sweden) is combining  $R'_w$  with the spectrum adaptation term for the low frequency range ( $C_{50-3150}$ ). Besides the weighted apparent sound reduction index, the weighted standardized level difference  $D_{nT,w}$  is employed in 10 European countries (in some of them it is together with the spectrum adaptation terms but only for the standard frequency range) [1].

COST Action TU0901 suggested to use the weighted standardized level difference  $D_{nT,w}$  with the spectrum adaptation term  $C_{50-3150}$  for the classification of the airborne sound insulation. There are also many studies proposing various improvements of current sound insulation evaluation scheme with respect to more accurate assessment of lightweight structures in particular, e.g. [3] and [4].

Important issue is the improvement of methods for the estimation of the airborne sound insulation in order to achieve higher prediction reliability for timber frame structures. The tricky part is especially to estimate the TL in the frequency region below 100 Hz.

## FUNDAMENTAL THEORY

The paper is concerned with the TL of timber frame structures consisted of gypsum panels with wood studs and damped cavity. Besides timber frame structures, massive structures from solid wood are available on market. However, such structures can be approximated as single walls from the point of view of the TL. Very specific chapter is the field of triple leaf walls whose TL is quite challenging to estimate because of multiple resonances.

Three important frequencies have to be taken into account for double walls: the acoustic resonance  $f_2$  expressing the first occurrence of the standing wave pattern in the gap between panels, the mechanical resonance of the structure  $f_0$  and the limiting frequency related to the gap between panels  $f_l$  [5].

The structural mechanical resonance should be, in the best case, below the sound insulation spectrum [6]. This rule is possible to keep for the standard insulation frequency spectrum but not so easy to keep for the extended frequency spectrum. The fundamental mechanical resonance  $f_0$  [Hz] can be calculated [7]:

$$f_0 = \frac{1}{2\pi} \left( \frac{1.8 \rho_0 c_0^2 (m_1 + m_2)}{d m_1 m_2} \right)^{1/2} \quad (1)$$

where  $\rho_0$  [kg/m<sup>3</sup>] is the air density,

where  $c_0$  [m/s] is the sound speed in the air,

where  $m_1$  [kg/m<sup>2</sup>] and  $m_2$  [kg/m<sup>2</sup>] are the panel surface mass densities,

where  $d$  [m] is the gap thickness.

The constant 1.8 in Eq. 1 is obviously empirical and it is introduced by Sharp in Ref. [8] in order to obtain better agreement with experimental results. On the contrary, Davy in Ref. [9] does not use this constant.

The fundamental acoustic resonance expresses that half of the wavelength is equal to the gap width. The standing wave pattern can be eliminated by usage of the sound absorbing material which provides an attenuation inside the gap and does not form a mechanical bridge between panels [5]. The fundamental acoustic resonance  $f_2$  [Hz] is calculated as:

$$f_2 = \frac{c_0}{2d} \quad (2)$$

The limiting frequency  $f_l$  [Hz] has no special physical meaning but it formulates the border line between low frequency and high frequency behavior inside the air cavity [10]. It is also called the cross-over frequency and it is calculated as follows [5]:

$$f_l = \frac{c_0}{2\pi d} \quad (3)$$

The TL of a double leaf structure is highly dependent on the fact whether there is mechanical coupling inside the cavity (e.g. wood studs) and consequently, whether there is structure-borne transmission through the cavity. The TL for frequencies  $f < f_0$  and for the case of a wall with two leafs which are acoustically and mechanically isolated is calculated [11] as:

$$R = 20 \log \left( \frac{\omega (m_1 + m_2)}{2 \rho_0 c_0} \right) - 5.5 \quad (4)$$

where  $R$  [dB] is the transmission loss of a double leaf structure,

where  $\omega$  [rad/s] is the angular frequency.

Eq. 4 basically says that the TL of double leaf walls is for frequencies  $f < f_0$  estimated according to the mass law with the sum of surface mass densities of partial panels. The TL can be calculated for frequencies  $f_0 < f < f_l$  as [11]:

$$R = R_1 + R_2 + 20 \log(2k d) \quad (5)$$

where  $k$  [ $m^{-1}$ ] is the wave number,

where  $R_1$  and  $R_2$  [dB] are the transmission losses of partial panels.

The gap thickness is not important parameter for high frequencies as it can be seen from following Eq. 6. The TL can be calculated for  $f > f_l$  as [11]:

$$R = R_1 + R_2 + 6 \quad (6)$$

However, the achieved TL is significantly lower when panels are mechanically connected via point or line connections. The decrease of the TL of a structure with studs occurs above the bridging frequency which expresses the structure-borne conduction limits of used connections. The bridging frequency can be found either graphically or with equations of the analytical geometry. It is also important to notice that a dip in the TL occurs around the critical frequency when the wavelength of the bending wave in the structure equals to the trace wavelength of the incident sound wave at the grazing angle [5].

## CASE STUDIES

Case studies of three timber frame structures are presented in this chapter. Experimental data is taken from a report published by the National Research Council of Canada [12]. Davy claimed that the experimental data contained in this report is at the lower end of the measurement results from outside of Australia [9].

Sharp’s method used in case studies was published in Ref. [8], [11] and reviewed in Ref. [5]. Davy’s method was published in Ref. [13], [14], [15] and reviewed in Ref. [5]. All calculations in this paper were executed by Matlab scripts programmed by the author.

Gypsum boards are modelled with these properties:

- Young modulus:  $E = 2.0 \cdot 10^9$  Pa [5],
- Total loss factor:  $\eta_{TOT} = 0.1$  [5],
- Length of the opening:  $l_x = 3.05$  m [12],
- Height of the opening:  $l_y = 2.44$  m [12].

Young modulus is used together with the surface mass density and the thickness to calculate the longitudinal speed of sound waves. The surface mass density of gypsum boards and the overall wall composition vary for different case studies. Obviously, there is uncertainty in input parameters, especially in the total loss factor.

### Asymmetric timber frame wall

The first case study is an asymmetrically sheathed timber frame wall depicted in Fig. 1. The TL calculated after Sharp and Davy along with the experimental data is shown in Fig. 2.

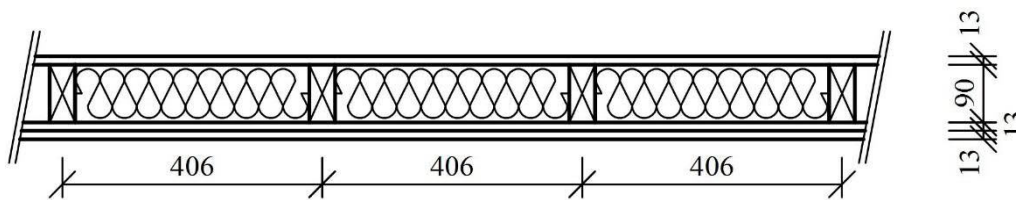


Fig. 1: Geometry of the asymmetrically sheathed timber frame wall (dimensions in mm)

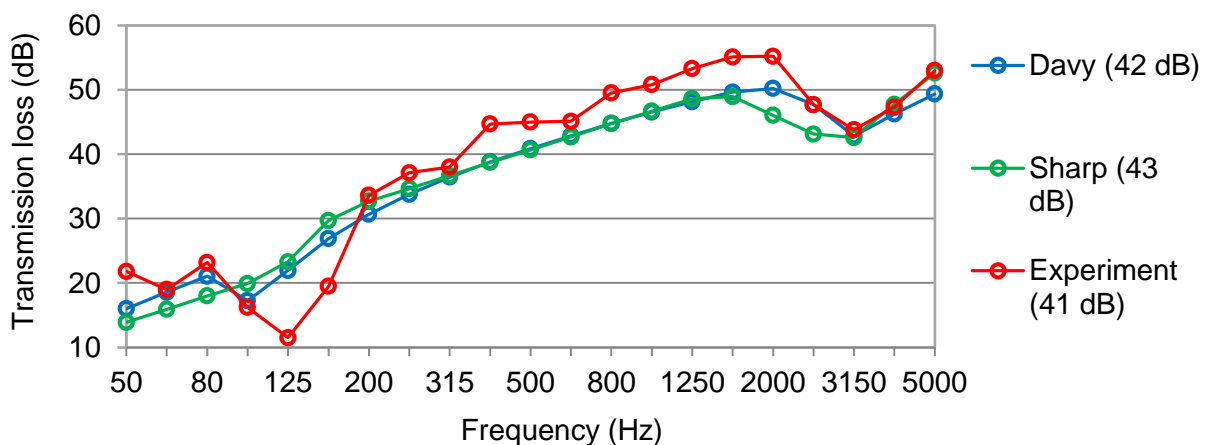


Fig. 2: The TL of the asymmetrically sheathed timber frame wall as a function of the frequency obtained with Davy’s and Sharp’s methods and an experiment (performed in Ref. [12]) with  $R_w$  in parenthesis

While the dip at the critical frequency is estimated very well, the dip around 125 Hz is poorly predicted. The TL is underestimated between the bridging frequency and the critical frequency and so the methods seem to be on the safe side in the middle frequency range.

Line-line rigid connections are modeled by both methods. The surface mass density of one gypsum board is 8.3 kg/m<sup>2</sup>. Gypsum boards are connected with screws and frictional losses can occur between the boards screwed together. Still, applied methods estimate the weighted sound reduction index with a reasonable precision.

### Wood studs with resilient channels

The second case study deals with modeling of resilient channels attached to the wood studs on both sides. Geometry of the case study is shown in Fig. 3. The TL calculated with Sharp's and Davy's method together with the test results is shown in Fig. 4.

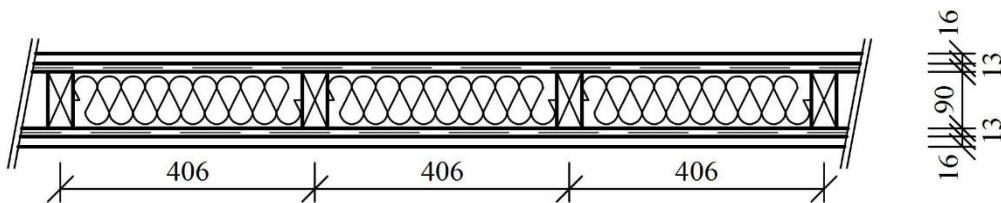


Fig. 3: Geometry of the timber frame wall with resilient channels on both sides (dimensions in mm)

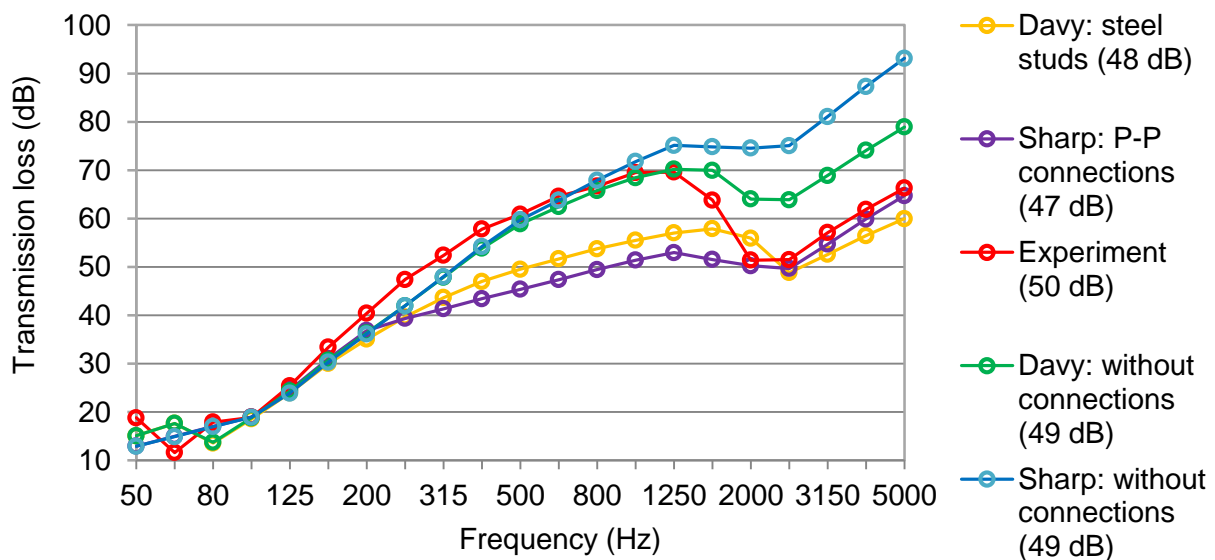


Fig. 4: The TL of the timber frame wall with resilient channels on both sides as a function of the frequency obtained with Davy's and Sharp's methods and an experiment (performed in Ref. [12]) with  $R_w$  in parenthesis

The gap width is 116 mm in total (90 mm plus two times 13 mm for resilient channels). The wall is symmetrically sheathed with one gypsum board on each side (surface mass density 11.1 kg/m<sup>2</sup>). Spacing of resilient channels is 610 mm. Sharp's method is calculated both with point-point connections and with acoustically and mechanically isolated panels. Davy's method models steel

studs (compliance  $C_M = 10^{-6} \text{ m}^2 \text{ N}^{-1}$  [13]) and a point support of the second panel (after Fahy [7]). The second calculation with Davy's method models a wall without any structure-borne sound transmission (sound is transmitted only through the damped cavity).

Fig. 4 shows that the TL is estimated fairly well in the domain of low frequencies and reasonably well in the domain of medium frequencies by Davy and Sharp (both without any connections). Still, the TL around the critical frequency is poorly estimated by the calculations with mechanically isolated panels. Apparently, resilient channels cause the structure-borne transmission similar to the point-point supports above the critical frequency.

### Staggered wood studs

The third case study investigates a double leaf wall with staggered wood studs. Geometry of the timber frame wall with staggered studs is shown in Fig. 5. The TL calculated with Sharp's and Davy's method along with the test results is shown in Fig. 6.

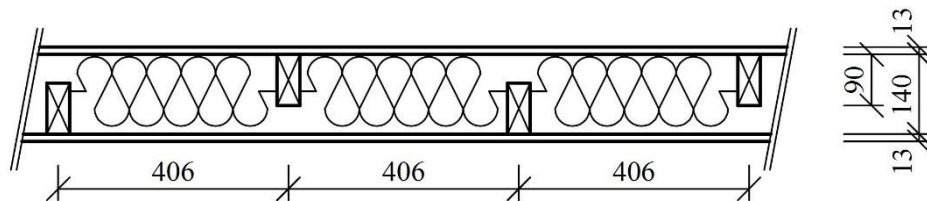


Fig. 5: Geometry of the timber frame wall with staggered studs (dimensions in mm)

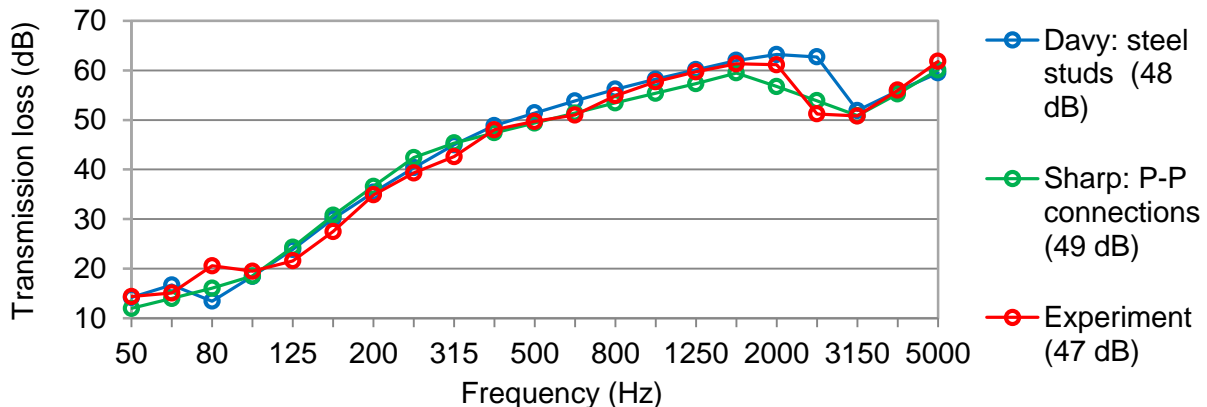


Fig. 6: The TL of the timber frame wall with staggered studs as a function of the frequency obtained with Davy's and Sharp's methods and an experiment (performed in Ref. [12]) with  $R_w$  in parenthesis

The surface mass density of a gypsum board is  $10.0 \text{ kg/m}^2$ . Davy's method employs steel studs (compliance  $C_M = 10^{-6} \text{ m}^2 \text{ N}^{-1}$  [13]) and a point support of the second panel (after Fahy [7]). Spacing of connections entered in the calculation was doubled (812 mm).

Surprisingly, models with steel studs (after Davy) and P-P connections (after Sharp) estimate the TL of the timber frame wall very well. It is possible to draw a conclusion that even though staggered studs do not form a mechanical bridge between gypsum panels, they cause change in the sound propagation inside the cavity. In this case estimation methods are slightly over predicting the weighted sound reduction index.

## SINGLE NUMBER QUANTITIES FOR THE EVALUATION OF THE SOUND INSULATION

Single number quantities are suitable for the evaluation of the sound insulation of traditionally used heavy-weight structures, e.g. concrete and masonry walls, as it is shown in this section. Experimental data for the investigated concrete wall was published in Ref. [18].

The examined wall is constituted from solid concrete blocks with these properties:

- Thickness:  $t = 140$  mm [18],
- Surface mass density:  $m = 300.7$  kg/m<sup>2</sup> [18],
- Internal loss factor:  $\eta_{INT} = 0.006$  [17],
- Longitudinal speed of sound waves:  $c_L = 3500$  m/s [17].

An application of estimation methods for single walls is also demonstrated. Watters's method was published in Ref. [16] and reviewed in Ref. [6]. EN 12354-1 was described in the standard [17]. The total loss factor is calculated for the laboratory conditions with an equation from Ref. [17]. Since the structure was tested by the same research council, test opening dimensions are regarded to be identical to previous timber frame structures.

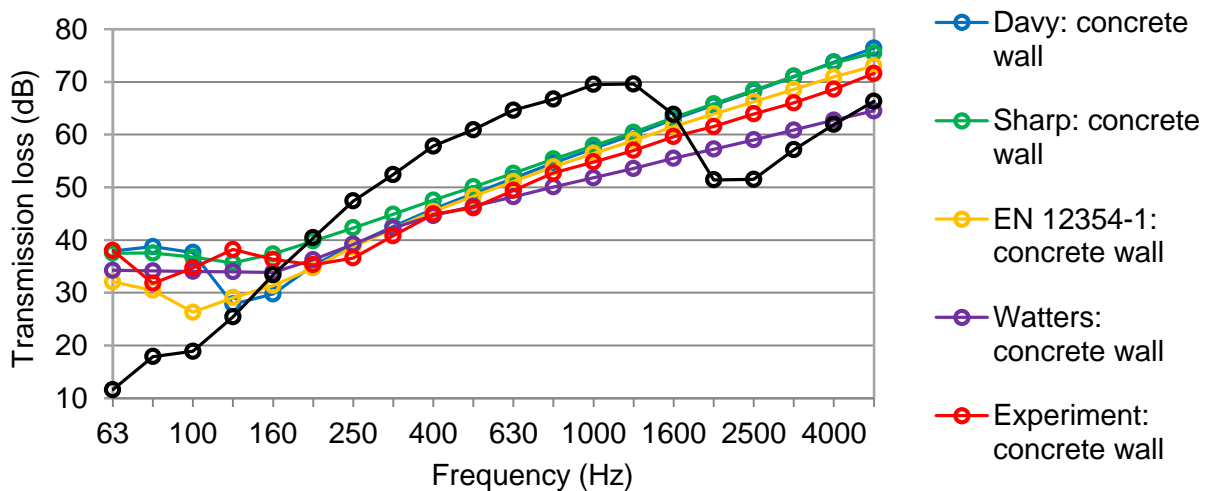


Fig. 7: The TL of the concrete wall and the timber frame wall with resilient channels as a function of the frequency obtained with different methods and experiments (performed in Ref. [12] and [18]). The black curve represents experimental outputs for the object of measurements, i.e. the timber frame wall

The TL of the timber frame structure with resilient channels (see Fig. 3) is compared to calculated and measured TL of the concrete wall. Results of the comparison are presented in Fig. 7 and single number quantities  $R_w$ ,  $C$  and  $C_{tr}$  are presented in Tab. 1.

Tab. 1: Single number quantities for the evaluation of the sound insulation

Indicators	Davy: concrete wall	Sharp: concrete wall	EN 12354-1: concrete wall	Watters: concrete wall	Experiment: concrete wall	Experiment: timber frame wall
$R_w$	50	53	49	50	50	50
$C$	-2	-1	-2	-2	-1	-5
$C_{tr}$	-7	-5	-7	-5	-5	-12

## CONCLUSIONS

The last section of this paper demonstrated that the design of the sound insulation of timber frame structures introduces different issues than the design of traditional heavy-weight structures. On the other hand, Fig. 7 showed that the precise estimation of the TL in the low frequency range is still a challenge even for a concrete block wall.

In spite of the fact that the weighted sound reduction index is the same for a concrete wall and a timber frame wall, the spectrum adaptation terms are quite different. It is also appropriate to remark that only the standard frequency range was evaluated. The spectrum adaptation terms for the extended frequency range would give even higher differences.

The estimation of the TL of a timber frame wall is a complex procedure because of many possible wall compositions (resilient channels on one or two sides, staggered or double studs, differently damped cavity etc.). Responsible acoustician should in practice collect all possible data about the designed structure and also about similar structures which were already tested.

## ACKNOWLEDGEMENTS

This work has been supported by the Ministry of Education, Youth and Sports within National Sustainability Programme I (NPU I), project No. LO1605 - University Centre for Energy Efficient Buildings – Sustainability Phase.

## REFERENCES

- [1] Rasmussen, B., Machimbarrena, M. (editors), 2014. Building acoustics throughout Europe Volume 1: Towards a common framework in building acoustics throughout Europe. COST Action TU0901, ISBN: 978-84-697-0158-4.
- [2] ISO 717-1: Acoustics, 2013. Rating of sound insulation in buildings and of building elements. Part 1: Airborne sound insulation. CEN.
- [3] Muellner, H., Frey, A., Humer, C., 2008. Sound insulation properties of building elements, considering the frequency range below 100 Hz. The Journal of the Acoustical Society of America, 123(5): 3766.
- [4] Muellner, H., Humer, C., Stani, M. M., 2007. Lightweight Building Elements with Improved Sound Insulation, Considering the low Frequency Range. In: 3rd Congress of the Alps Adria Acoustics Association. Austria.

- [5] Bies, D. A., Hansen, C. H., 2003. Engineering Noise Control: Theory and Practice, Third Edition. CRC Press, ISBN 978-0-41-526714-4.
- [6] Kaňka, J., 2007. Stavební fyzika 1: Akustika budov. Praha, ČVUT v Praze, ISBN 978-80-01-03664-8.
- [7] Fahy, F. J., 1985. Sound and Structural Vibration: Radiation, Transmission and Response. London, Academic Press, ISBN 0-12-247670-0.
- [8] Sharp, B. H., 1973. A Study of Techniques to Increase the Sound Installation of Building Elements. Wylie Laboratories, Report WR 73-S, Washington, DC, under contract H-1095.
- [9] Davy, J., 2009. Predicting the sound insulation of walls. Building Acoustics, vol. 16, no. 1, pp. 1-20.
- [10] Jacobsen, F. et al., 2011. Fundamentals of Acoustics and Noise Control. Department of Electrical Engineering, Technical University of Denmark, Note no 31200.
- [11] Sharp, B. H., 1978. Prediction Methods for the Sound Transmission of Building Elements, Noise Control Engineering 11, pp. 55-63.
- [12] Halliwell, R. E., Nightingale, T. R. T., Warnock, A. C. C., Birta, J. A., 1988. Gypsum Board Walls: Transmission Loss Data. Internal Report IRC-IR-761. Institute for Research in Construction, National Research Council of Canada. Ottawa.
- [13] Davy, J. L., 1990. Predicting the Sound Transmission Loss of Cavity Walls. In: Interior Noise Climates - Proceedings of the 1989/90 National Conference of the Australian Acoustical Society, Australian Acoustical Society, Perth, Australia.
- [14] Davy, J. L., 1991. Predicting the Sound Insulation of Stud Walls. In: The Costs of Noise - Proceedings of Inter-Noise 91 Conference, Volume 1, 251–254, Australian Acoustical Society, Sydney.
- [15] Davy, J. L., 1993. The Sound Transmission of Cavity Walls due to Stud. In: People Versus Noise - Proceedings of the Inter-Noise 93 Conference, Volume 2, 975–978, Belgium Acoustical Association, Leuven.
- [16] Kurtze G., Watters B. G., 1959. New wall design for high transmission loss or high damping. Journal of Acoustic Society of America 31, s. 739-748.
- [17] ČSN EN 12354-1: Building acoustics, 2001. Estimation of acoustical performance of buildings from the performance of elements. Part 1: Airborne sound insulation between rooms.
- [18] Warnock, A. C. C., 1990. Sound Transmission Loss Measurements Through 190 mm and 140 mm Blocks With Added Drywall and Through Cavity Block Walls. National Research Council Canada, Institute for Research in Construction. Internal Report No. 586.



# FLUCTUATION EFFECT OF EQUILIBRIUM MOISTURE CONTENT OF LOW SUBGRADE UNDER HIGH GROUNDWATER LEVEL IN HOT AND HUMID CLIMATIC REGIONS

*Que Yun<sup>1</sup>, Wu Jiabin<sup>2</sup>*

1. *University of Fuzhou, Faculty of Civil Engineering, Fuzhou, Fujian, China; queyun\_2001@tom.com*

2. *University of Fuzhou, Faculty of Civil Engineering, Fuzhou, Fujian, China; 441971785 @QQ.com*

## ABSTRACT

In order to reveal the fluctuation effect of equilibrium moisture content of low subgrade in hot and humid climatic regions, the effect of temperature on the fluctuation of the equilibrium moisture content of subgrade was analysed. Taking the typical climate and the subgrade soil in Fujian province as an example, three technological methods - theoretical analysis, numerical simulation and indoor simulation experiment - were adopted in the investigation of the fluctuation effect of equilibrium moisture content of subgrade. The results show that, computing results from the formula of the equilibrium moisture content of subgrade, the numerical simulation results are closer to each other in consideration of the temperature effect. The test results can not reflect the relationship between the equilibrium moisture content and the height of embankment. The maximum fluctuation range of the equilibrium moisture content of the cement concrete pavement is less than 2 percent in Fujian area, and this phenomenon presents the effect of the moist-hot climate on the equilibrium moisture content. Equilibrium moisture content presents a declining trend with the increment of the temperature and the compactness. So, if matric potential considering temperature indirectly reflects the influence of thermal potential, then the equilibrium moisture content of low subgrade under high groundwater level can be estimated approximately. The fluctuation range of equilibrium moisture content in different layers of subgrade can be reduced effectively with the increment of the roadbed compaction degree.

## KEYWORDS

High groundwater level, low subgrade, equilibrium moisture content, fluctuation effect, hot and humid climatic regions

## INTRODUCTION

In China, low subgrades exist widely in soft soil areas due to its small land occupation. It is well known that a moisture content of subgrade soil is close to the optimum moisture content during the filling construction of subgrade. The moisture content near the centre of the subgrade will present seasonal variation because of factors such as the fluctuation of groundwater level and traffic load and it can reach equilibrium moisture content within about 5 years. Therefore, the design parameters of subgrade under equilibrium moisture content conditions are much more suitable for the long-term performance of subgrade.





In light of this background, many scholars have made further research on the equilibrium moisture content of subgrade. Furthermore, a large amount of achievements have been obtained in this field, such as the equation for prediction of equilibrium moisture content in the subgrade based on field monitoring data [1-2], the equilibrium moisture content of subgrade obtained by test of mould of water curing [3-4], and the prediction method of equilibrium moisture content of unsaturated clay subgrade outside the affected zone of atmospheric precipitation/evaporation based on a single-valued function relationship between moisture content and matric suction of soils [5-6].

All of these results have important significance for perfecting the durability design method of subgrade, but there is limited information on the effect of temperature on the equilibrium moisture content of subgrade.

However, it is known that changes of air temperature in different seasons will lead to a change of suction, and the temperature characteristics of suction play an important role in the pavement-subgrade system. For example, annual variation of measured temperature of roadbed in Nanping City of China is about 25 °C. Even so, how they influence the fluctuation effect of equilibrium moisture content of roadbed is still unknown. To address these issues, this paper takes a typical hot and humid climatic region in Fujian province of China as an example, and the fluctuation effect of equilibrium moisture content of subgrade in this zone is analysed based on the combination of theoretical analysis, numerical simulation and indoor simulation experiment.

## PREDICTION OF EQUILIBRIUM MOISTURE CONTENT OF SUBGRADE CONSIDERING THE TEMPERATURE EFFECT

### Soil-Water Potential Principle of Subgrade Under High Groundwater Level Condition

According to the theory of soil water potential, soil water potential consists of five parts: matric potential, gravitational potential, solute potential, pressure potential and temperature potential. In general, pressure potential of unsaturated soil is equal to zero and solute potential of unsaturated soil may not be considered. Because it is very difficult for the temperature potential to be stated by a mathematical formula, the matric potential considering the temperature effect is used to indirectly reflect the effect of temperature on soil water potential in this paper. As shown in Fig. 1, the matric potential of subgrade will lead to a rise of the capillary water. Finally, when the moisture content of subgrade reaches equilibrium state, then the total soil-water potential under different depth of subgrade should be equal. If the base level is groundwater, the total soil-water potential of subgrade should be zero. So, the total soil-water potential of subgrade at point A can be described by:

$$\psi = \psi_m + \psi_g = 0 \quad (1)$$

Where,

$\psi$  ---the total soil-water potential, m;

$\psi_m$  ---the matric potential, m;

$\psi_g$  ---the gravity potential, m.



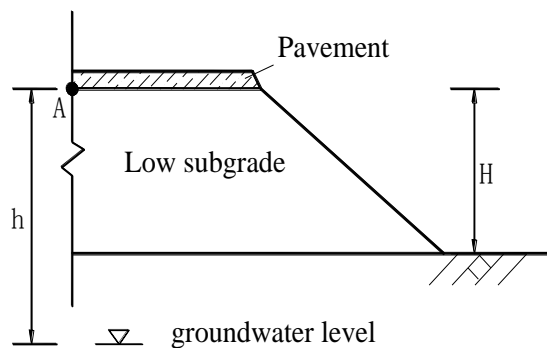


Fig. 1. - Typical Cross Section

### The Matric Potential Considering the Temperature Effect

Three different types of granite residual soil in Fujian province of China were chosen for test research on soil-water characteristic curve. Physical properties of granite residual soil are shown in Tab. 1.

Tab. 1. - Physical Properties of Granite Residual Soil

Soil Sample	Particle Composition (%)				Maximum Dry Density g·cm <sup>-3</sup>	Optimum Moisture Content %	Specific Gravity -	Liquid Limit %	Plastic Limit %	Plastic Limit Index -
	>2 mm	2~0.075 mm	0.002~0.075 mm	<0.002 mm						
I	22.22	24.36	37.13	16.29	1.76	14.7	2.64	40.48	18.36	22.12
II	13.54	50.78	25.32	10.36	1.83	13.5	2.60	46.82	22.78	24.04
III	8.00	31.56	39.42	21.02	1.71	17.7	2.55	60.12	33.47	26.65

The filter paper test was used to determine soil-water characteristic curve [5]. The test data of seven soil samples will determine the relationship between the moisture content and the matric suction. Each type soil of test consists of four different temperature conditions (5 °C, 20 °C, 30 °C, and 45 °C). According to the test data, the Van Genuchten Model was used to fit the relationship between the moisture content and the matric suction of soils. It can be described by [7]:

$$\theta = \frac{\theta_s - \theta_r}{\left[ (a\psi_m)^n + 1 \right]^m} + \theta_r \quad (2)$$

Where,

$\theta$  ---the moisture content, %;

$\theta_s$  ---the saturated water content, %;

$\theta_r$  ---the residual water content, %;

a---the fitting parameter of soil-water characteristic curve, 1/cm;

m, n---the fitting parameters of soil-water characteristic curve,  $m=1-1/n$ .



The Fitting parameters of Van Genuchten Model of three soil samples are shown in Tab. 2.

Tab. 2. - Fitting Parameters of Van Genuchten Model of Three Soil Samples

Soil Sample	Temperature(°C)	a(1/cm)	n	$\theta_r$ (%)	$\theta_s$ (%)	Residual Sum of Squares
Soil sample I	5	0.4343	1.1843	2.51	24.91	1.0456E-4
	20	0.4980	1.2214	2.43	26.83	7.3821E-4
	30	0.1385	1.2531	2.3	24.98	8.8935E-4
	45	0.1317	1.1473	3.10	25.86	4.5761E-4
Soil sample II	5	0.5935	1.1617	2.19	25.83	1.6514E-4
	20	0.1720	1.2279	3.97	25.19	6.4134E-4
	30	0.4655	1.1731	3.9	25.31	2.9543E-4
	45	0.2021	1.2519	2.46	24.25	6.4099E-4
Soil sample III	5	0.0299	1.1903	4.97	27.18	8.45098E-5
	20	0.0011	1.5485	3.62	25.03	4.8977E-4
	30	0.0084	1.2663	2.5	25.63	3.1787E-5
	45	0.0030	1.3270	6.52	25.68	2.309E-4

It can be seen from Tab. 2 that the model has high fitting accuracy, since the residual sum of squares of fitting is less than 0.001. Many studies show that the influence of temperature on soil-water characteristic curve of unsaturated soil should not be neglected. It is found that there is a power function relationship between temperature and parameters of Van Genuchten model based on the thermodynamics principle[8]. Using the method above, the relationship between temperature and parameters of Van Genuchten model was built based on the data in Tab. 2. It can be described by:

Soil sample I:

$$\begin{cases} a = 8E-05T^3 - 0.0058T^2 + 0.1088T + 0.0252 & R^2 = 1 \\ n = -1E-05T^3 + 0.0006T^2 - 0.0075T + 1.2075 & R^2 = 1 \\ \theta_r = 7E-05T^3 - 0.0044T^2 + 0.0652T + 2.284 & R^2 = 1 \\ \theta_s = 0.0006T^3 - 0.0431T^2 + 0.9142T + 21.348 & R^2 = 1 \end{cases} \quad (3)$$

Soil sample II:

$$\begin{cases} a = -0.0001T^3 + 0.008T^2 - 0.1743T + 1.2769 & R^2 = 1 \\ n = 2E-05T^3 - 0.0015T^2 + 0.0318T + 1.0382 & R^2 = 1 \\ \theta_r = 4E-05T^3 - 0.007T^2 + 0.2755T + 0.984 & R^2 = 1 \\ \theta_s = -0.0001T^3 + 0.0097T^2 - 0.2141T + 26.674 & R^2 = 1 \end{cases} \quad (4)$$

Soil sample III:

$$\begin{cases} a = -4E-06T^3 + 0.0003T^2 - 0.0077T + 0.0613 & R^2 = 1 \\ n = 8E-05T^3 - 0.0067T^2 + 0.1477T + 0.6094 & R^2 = 1 \\ \theta_r = 0.0004T^3 - 0.023T^2 + 0.2737T + 4.126 & R^2 = 1 \\ \theta_s = -0.0003T^3 + 0.0224T^2 - 0.5677T + 29.49 & R^2 = 1 \end{cases} \quad (5)$$



The equilibrium moisture content of subgrade considering the temperature effect can be approximately predicted by Equation (2).

## NUMERICAL SIMULATION OF EQUILIBRIUM MOISTURE CONTENT OF SUBGRADE Hydrothermal Modelling

Hydrothermal modelling can be described by [9] [10]:

$$\begin{cases} \frac{\partial \theta}{\partial t} = \frac{\partial}{\partial z} \left( D(\theta, T) \frac{\partial \theta}{\partial z} \right) + \frac{\partial}{\partial z} \left( D_r \frac{\partial T}{\partial z} \right) - \frac{\partial k(\theta, T)}{\partial z} \\ \rho c_v(\theta) \frac{\partial T}{\partial t} = \lambda_n(\theta) \left( \frac{\partial^2 T}{\partial z^2} \right) \end{cases} \quad (7)$$

Where,

$T$ ---the temperature, °C;

$D(\theta, T)$  --- the moisture diffusion coefficient considering temperature effect, cm<sup>2</sup>/min;

$D_r$  --- the moisture diffusion coefficient considering temperature gradient effect, cm<sup>2</sup>/ (min.°C) ;

$k(\theta, T)$  ---the hydraulic conductivity considering the temperature effect, cm/min;

$c_v(\theta)$  ---the specific heat capacity considering temperature effect, J/(kg.°C);

$\lambda_n(\theta)$  ---the thermal conductivity considering moisture effect, W/(m.°C) .

The finite difference model is adopted to solve the hydrothermal modelling based on alternating direction implicit method. Implicit differential scheme of Equation (7) can be described by [9]:

$$\begin{cases} \frac{\theta_i^{k+1} - \theta_i^k}{\Delta t} = D_{i+1/2}(\theta, T) \frac{\theta_{i+1}^{k+1} - \theta_i^{k+1}}{\Delta z^2} + D_{i-1/2}(\theta, T) \frac{\theta_{i-1}^{k+1} - \theta_i^{k+1}}{\Delta z^2} - \frac{k_{i+1/2}^k(\theta, T) - k_{i-1/2}^k(\theta, T)}{\Delta z} \\ \frac{T_n^{i+1} - T_n^i}{\Delta t} = \frac{T_{n+1}^i + T_{n-1}^i - 2T_n^i}{\Delta z^2} \frac{\lambda_k(\theta)}{\rho c_v(\theta)} \end{cases} \quad (8)$$

The height of the numerical model is 5 m. According to its basic ideology, the analysis is conducted using MATLAB.



## Material Parameters

The material parameters in the numerical model are shown in Tab. 3 and Tab. 4. Tab. 3 shows the thermal parameters of cement concrete pavement which is simplified as a single layer, and Tab. 4 shows the hydrothermal parameters of subgrade considering the temperature effect.

Tab. 3. - Thermal Parameters of Cement Concrete Pavement [11]

Thermal Conductivity (W/m·°C)	Density (g·cm <sup>-3</sup> )	Heat Capacity (J/kg·°C)	Solar Radiation Absorption Rate	Pavement Emissivity	Stefan-Boltzmann Constant (J/s·m <sup>2</sup> ·K <sup>4</sup> )
1.5	2.4	900	0.75	0.85	5.67E-8

Tab. 4. - Hydrothermal Parameters of Subgrade [11]

Soil Sample	Water Diffusivity (cm <sup>2</sup> /min)	Diffusion Coefficient of Hydrothermal (cm <sup>2</sup> /min·°C)	Hydraulic Conductivity (cm/min)	Specific Heat Capacity (J/kg·°C)	Thermal Conductivity (W/m·°C)
I	$0.14\chi\left(\frac{\theta}{0.36}\right)^{5.4}$	4.6E-5	$4.2E-4\alpha\left(\frac{\theta}{0.36}\right)^{2.9}$	$1.31K + 4.18\theta + 0.001$	$\frac{\lambda_a G_s \lambda_{ha} + (\lambda_w \lambda_{hw} - \lambda_a \lambda_{ha}) G_s \theta + (\lambda_m \lambda_{hm} - \lambda_a \lambda_{ha}) \rho_d K}{\lambda_a G_s + (\lambda_w - \lambda_a) G_s \theta + (\lambda_m - \lambda_a) \rho_d K}$
II	$0.26\chi\left(\frac{\theta}{0.31}\right)^{5.5}$	5.4E-5	$8.7E-5\alpha\left(\frac{\theta}{0.31}\right)^{3.2}$	$1.39K + 4.18\theta + 0.001$	
III	$0.02\chi\left(\frac{\theta}{0.35}\right)^{4.7}$	6.2E-5	$3E-5\alpha\left(\frac{\theta}{0.35}\right)^{3.1}$	$1.32K + 4.18\theta + 0.001$	

In Tab. 4, every symbol is expressed as follows:

$\chi$  ---the coefficient of diffusion considering temperature effect;

$\alpha$  ---the coefficient of hydraulic conductivity considering temperature effect;

$k$  ---the compactness of subgrade, 95%;

$\lambda_m$  ---the weighted coefficient of soil particle, soil sample I,  $\lambda_m = 0.33$ , soil sample II,  $\lambda_m = 0.27$ , soil sample III,  $\lambda_m = 0.28$ ;

$\lambda_w$  ---the weighted coefficient of water,  $\lambda_w = 1$ ;

$\lambda_a$  ---the weighted coefficient of air,  $\lambda_a = \frac{0.6321\theta + 0.2334}{1.8132\theta - 1.8962\theta^2 - 0.075}$ ;

$\lambda_{ha}$  ---the thermal conductivity of air, W/(m·°C);

$\lambda_{hw}$  ---the thermal conductivity of water, W/(m·°C);

$\lambda_{hm}$  ---the thermal conductivity of soil, W/(m·°C).



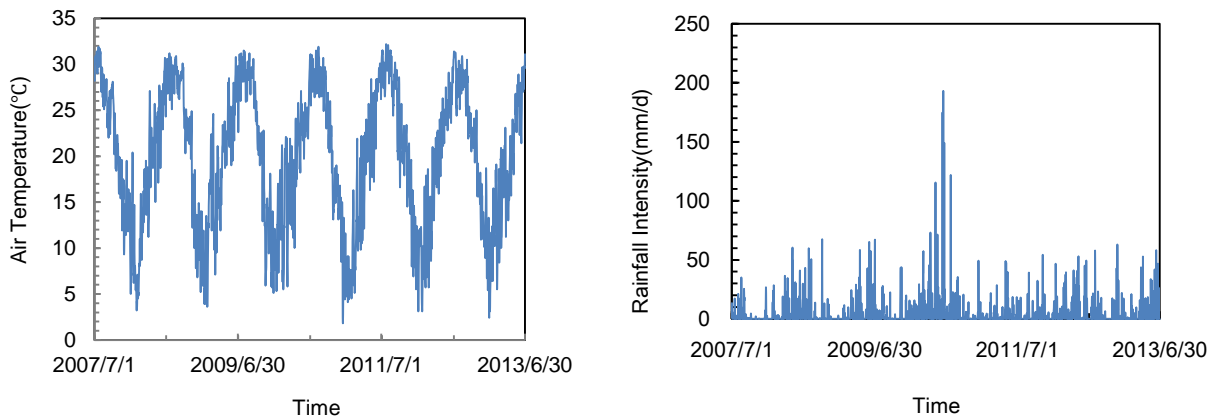
### The Initial and Boundary Condition

The boundary condition of the upper surface of subgrade is heat flux and an impervious boundary without considering the impact of evaporation.

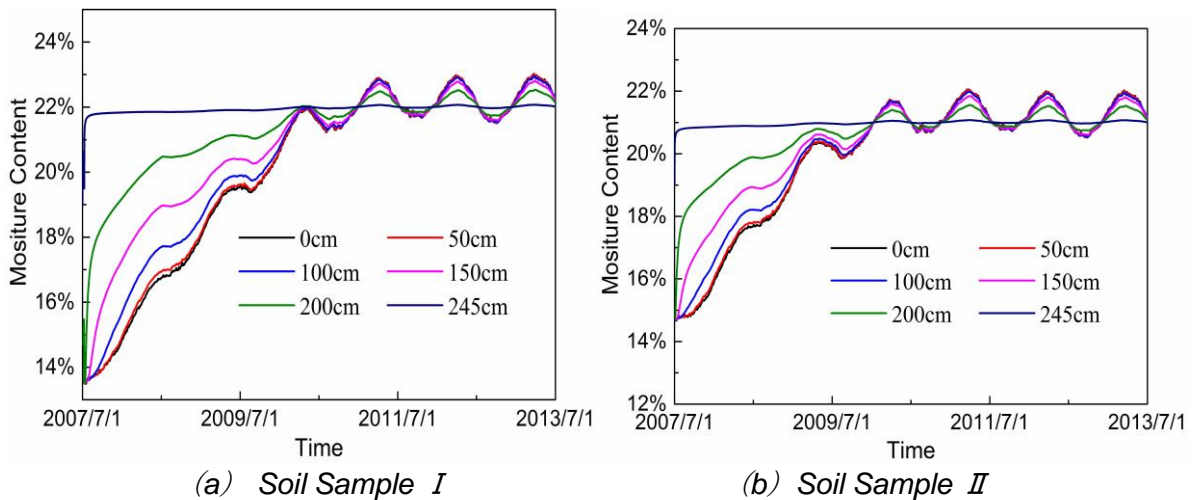
The initial moisture content of subgrade is the optimum moisture content and the initial temperature is the average atmospheric temperature (20°C). The depth of groundwater level is 2.5m.

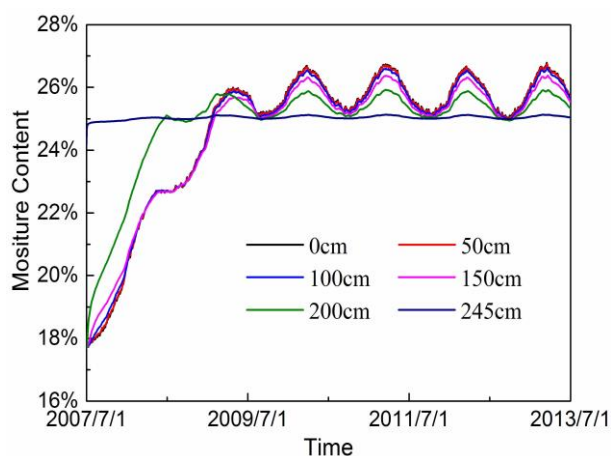
### Numerical Simulation Results Analysis

In order to calculate seasonal variation of the moisture content of subgrade, climate data in Nanping City of China were selected as the typical meteorological boundary. The air temperature from July 1, 2007 to June 30, 2013 is shown in Fig. 4. The calculation results for different depths are shown in Fig. 5.



(a) Air Temperature (b) Rainfall Intensity  
 Fig. 4. - Seasonal Variation of Meteorological Data in Nanping Area





(c) Soil Sample III

Fig. 5. Seasonal Variation of Moisture Content of Low Subgrade in Nanping Area

In Fig. 5, it can be seen that moisture content at different depths of three types of subgrade present an initial increasing and then fluctuation trend. The maximum fluctuation range of the equilibrium moisture content of the cement concrete pavement is less than 2 percent.

## THE TEST FOR EQUILIBRIUM MOISTURE CONTENT OF SOIL AT DIFFERENT TEMPERATURE CONDITIONS

### Test Procedures

A mould of water curing was used to simulate the impact of field environment condition on the equilibrium moisture of subgrade [3-4]. The test device is shown in Fig. 6.

The test procedures are as follows:

(1) Wet curing mould making

A mould with a diameter of 7cm and height of 19 cm is made using PVC material. There are holes around the wall of the mould. In order to prevent water loss, wood blocks are used in the two ends of mould.

(2) Sample preparation

First, soil samples with the optimum moisture content are compacted by six layers in order to ensure adequate soil compaction. The height of each layer of soil is about 3 or 4cm. Soil samples are compacted by compaction instrument. Second, the samples are encapsulated by a non-woven material with a thickness of 0.01mm. Third, the samples are placed in the mould. In order to prevent lateral expansion, a nut is used to secure the mould. Sample preparation is shown in Fig. (7).

(3) Accelerated saturation stage of the soil sample

When compaction is completed, the soil sample is weighed. In order to accelerate saturation of the soil, the samples are put into a bucket under different temperature conditions for three hours.

(4) Wet curing stage of the soil sample



In order to ensure that the soil samples will absorb water uniformly because of imbalance of potential energy, the mould sealed by plastic bags is placed in a constant temperature and humidity system with a relative humidity of 100% and different temperatures of 5 °C, 20 °C, 30 °C, 45 °C, respectively. The soil samples should be inverted every 12h to ensure the uniformity. The relative humidity and moisture of soil samples should be recorded every 24 hours until the weight of soil samples do not change in two days. The test period is about 7d to 14d.

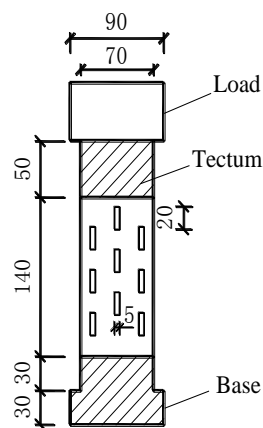


Fig. 6. - Mould of Water Curing (unit: mm)



Fig. 7. - Sample Preparation

## Results Analysis of Indoor Test

Tests for equilibrium moisture content of three types soil of table 1 were conducted under the different conditions of three compaction degrees (88%, 95%, 100%) and four temperatures (5 °C, 20°C, 30°C, 45°C). In order to reduce the errors, parallel tests of each test mode were conducted. The relationship curve of moisture content of soil sample I and time is shown in Fig 8. Tab. 3 shows the equilibrium moisture content of the three types of soil.

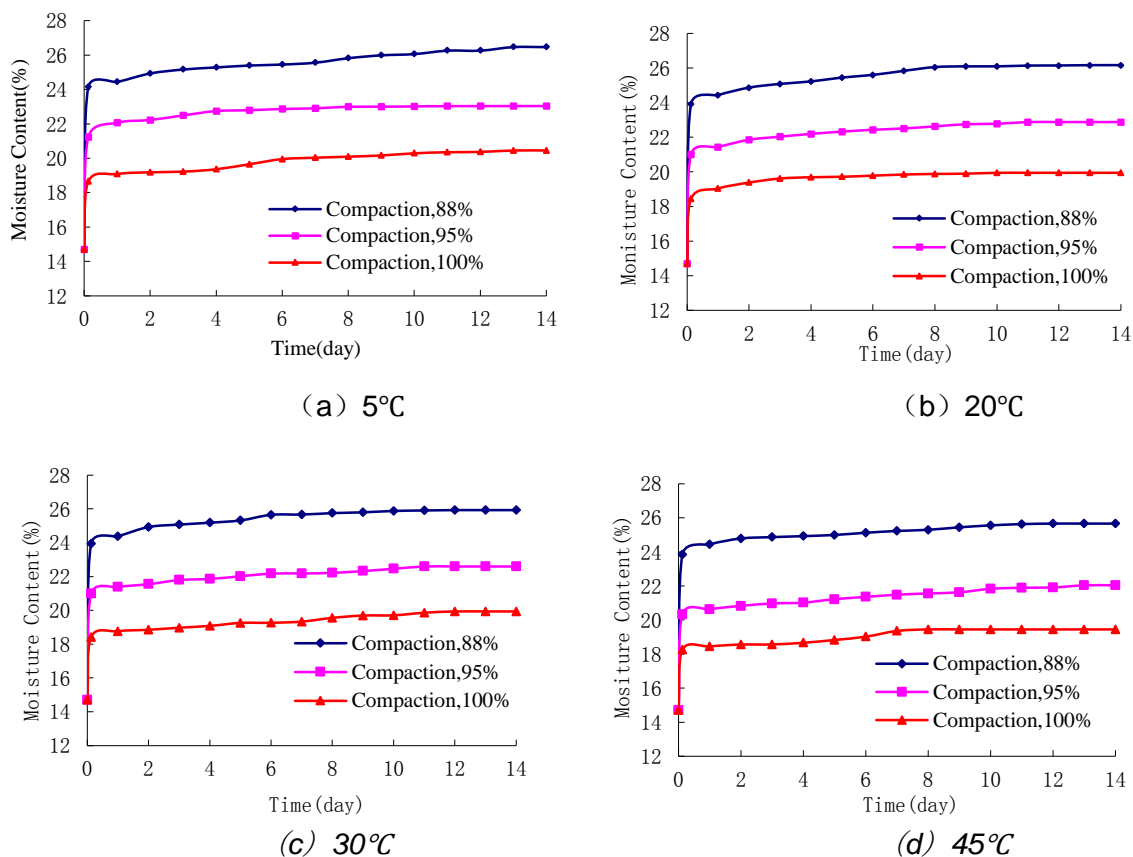


Fig. 8. - Time-dependent Curve of Moisture Content of Soil Sample I

Tab. 5 - Test Results of Equilibrium Moisture Content

Temperature(°C)	Compaction(%)	Soil sample I		Soil sample II		Soil sample III	
		Optimum Moisture Content (%)	Equilibrium Moisture Content (%)	Optimum Moisture Content (%)	Equilibrium Moisture Content (%)	Optimum Moisture Content (%)	Equilibrium Moisture Content (%)
5	88	14.7	26.47	13.5	24.76	17.7	28.44
	95	14.7	23.03	13.5	21.63	17.7	26.21
	100	14.7	20.45	13.5	19.96	17.7	21.74
20	88	14.7	26.16	13.5	24.47	17.7	26.95
	95	14.7	22.88	13.5	21.40	17.7	25.85
	100	14.7	19.95	13.5	19.15	17.7	20.23
30	88	14.7	25.93	13.5	24.27	17.7	27.85
	95	14.7	22.60	13.5	21.17	17.7	25.54
	100	14.7	19.93	13.5	18.99	17.7	21.64
45	88	14.7	25.66	13.5	24.20	17.7	26.13
	95	14.7	22.03	13.5	20.95	17.7	25.01
	100	14.7	19.45	13.5	18.56	17.7	20.53



In Fig. 5 and Tab. 5, it can be seen that the equilibrium moisture content of samples decreases with the increase of temperature. For example, the equilibrium moisture content of three soil samples decreases slightly when the temperature increased from 5 °C to 45 °C. Compaction has a great influence on the equilibrium moisture content. The equilibrium moisture content of samples decreases with the increase of the compaction. For example, the equilibrium moisture content of three soils decreases from 5% to 7% when the compaction of three soils increases from 88% to 100%.

It indicates that the increase of compaction of the subgrade can reduce the increase of equilibrium moisture content and improve the water stability of the subgrade.

### A COMPARISON ON DIFFERENT PREDICTIONS OF EQUILIBRIUM MOISTURE CONTENT

In order to contrast different predictions of equilibrium moisture content, the calculation results of formula which considering the temperature effect, numerical simulation and indoor test are shown in Tab. 6.

Tab. 6. - Prediction of Equilibrium Moisture Content of Different Soils

Soil Sample	Temperature (°C)	Formula Method (%)			Indoor Test (%)	Numerical Simulation (%)
		h=1m	h=2.5m	h=4m		h=2.5m
Soil sample I	5	23.83	23.46	21.47	23.03	21.10~22.81
	20	24.31	23.40	22.06	22.88	
	30	24.61	23.93	23.26	22.60	
	45	25.59	25.15	24.74	22.03	
Soil sample II	5	24.44	22.91	21.87	22.63	20.85~22.09
	20	24.77	24.03	23.35	22.40	
	30	24.26	22.96	22.04	22.17	
	45	23.70	22.75	21.89	21.95	
Soil sample III	5	27.13	27.02	26.91	26.21	25.01~26.60
	20	25.03	25.03	25.03	25.85	
	30	25.62	25.59	25.56	25.54	
	45	25.68	25.67	25.67	25.01	

From Tab. 6, the following conclusions can be drawn:

1. The equilibrium moisture content decreases with the increase of height of subgrade. This indicates that if the temperature potential is constant, the matric potential will decrease with the increase of gravitational potential and the soil tends to be more dry;
2. Although the equilibrium moisture content determined from the tests is close to formula method and numerical simulation, the test results cannot reflect the relationship between the equilibrium moisture content and the height of embankment. Therefore, the test method needs further improvement;
3. The annual variation of temperature of roadbed in Fujian province range from 8 °C to 28°C [11]. Although the numerical analysis method cannot obtain the moisture



content of subgrade at a specified temperature, the peak of equilibrium moisture content calculated by the numerical analysis method is close to the formula method considering the temperature effect where the temperature is 5 °C and 30 °C, and their quantitative difference is less than 1.5%. This indicates that if matric potential considering the temperature indirectly reflects the influence of thermal potential, the equilibrium moisture content of low subgrade under high groundwater level can be estimated approximately;

4. The results of the three methods show that the maximum fluctuation range of the equilibrium moisture content of the cement concrete pavement is less than 2 percent in Fujian area, and this phenomenon presents the effect of the moist-hot climate on the equilibrium moisture content.

## CONCLUSIONS

This paper presents a study on fluctuation effect of equilibrium moisture content of low subgrade under high groundwater level in hot and humid climatic regions. Based on this study, the following conclusions can be made:

- 1) Computing results from the formula of the equilibrium moisture content of subgrade, the numerical simulation results are closer to each other in consideration of the temperature effect. This indicates that if matric potential considering temperature indirectly reflects the influence of thermal potential, the equilibrium moisture content of low subgrade under high groundwater level can be estimated approximately.

- 2) Although the equilibrium moisture content from the test is close to the results of the formula method and numerical simulation, the test results can not reflect the relationship between the equilibrium moisture content and the height of embankment. Therefore, the test method needs further improvement.

- 3) The maximum fluctuation range of the equilibrium moisture content of the cement concrete pavement is less than 2 percent in Fujian area, and this phenomenon presents the effect of the moist-hot climate on the equilibrium moisture content.

- 4) Equilibrium moisture content presents a declining trend with the increment of the temperature and the compactness. Furthermore, the fluctuation range of equilibrium moisture content in different layers of subgrade can be reduced effectively with the increment of the roadbed compaction degree.

## ACKNOWLEDGEMENTS

This work was financially supported by the Natural Science Development Fund of Fuzhou University (2013-XQ-39).





## REFERENCES

- [1] S. Rao., 1997. Analysis of in-situ moisture content data for Arkansas subgrades, Ph.D. thesis, University of Arkansas, Fayetteville, Arkansas, America
- [2] C. W. Cao., 2007. Subgrade moisture condition and adjustment factors of resilient modulus, Ph.D. thesis, Tongji University, Shanghai, China
- [3] J. Uzan., 1998. Characterization of clayey subgrade materials for mechanistic design of flexible pavements, Transportation Research Board, vol. 1629, no. 1, pp. 189-196
- [4] S. R. Yang., 2005. Behavior of unsaturated subgrade soils under repeated loading, Ph.D. thesis, National Central University, Taipei, China
- [5] X. Qiu, Y. Qing, Q. L. You., 2013. Distribution Characteristics and Prediction of Equilibrium Moisture of Non-saturated Clay Subgrade, Journal of Civil, Architectural&Environmental Engineering, vol. 35, no. 2 , pp. 15-20
- [6] J. L. Zheng, R. Zhang., 2013. Prediction and Application of Equilibrium Water Content of Expansive Soil Subgrade, Proceedings of the Second International Conference on Geotechnical and Earthquake Engineering, 754-761.
- [7] M.Th.Van Genuchten., 1980. A Closed-Form Equation for Predicting the Hydraulic Conductivity of Unsaturated Soils. Soil Science Society of America Journal, vol. 44, no. 5, pp. 892-898
- [8] G. Q. Cai, C. G. Zhao and Y. Liu., 2012. Temperature effects on soil-water characteristic curve of unsaturated soils. Rock and soil mechanics, vol. 31, no. 4, pp. 1055-1060
- [9] Z. D. Lei, S. X. Yang and S. C. Xie., 1988. Soil Water Dynamics, Tsinghua University Press, pp. 107-114.
- [10] S. M. Yang and W. Q. Tao., 2006. Heat Transfer Theory, Beijing, Higher Education Press , pp. 122-132.
- [11] X.Q. Yao, 2011. Study on moisture migrate mechanism in granite eluvial soil embankment in moist heat areas , M.S. thesis, Fuzhou University, Fuzhou, China

## NUMERICAL MODEL APPLICATION IN ROWING SIMULATOR DESIGN

*Petr Chmátal<sup>1</sup>, Jaroslav Pollert<sup>2</sup> and Ondřej Švanda<sup>3</sup>*

1. *Czech Technical University in Prague, Faculty of Civil Engineering, Department of Sanitary and Ecological Engineering, [petr.chmatal@fsv.cvut.cz](mailto:petr.chmatal@fsv.cvut.cz)*
2. *Czech Technical University in Prague, Faculty of Civil Engineering, Department of Sanitary and Ecological Engineering, [pollertj@fsv.cvut.cz](mailto:pollertj@fsv.cvut.cz)*
3. *Czech Technical University in Prague, Faculty of Civil Engineering, Department of Sanitary and Ecological Engineering, [ondrej.svanda@fsv.cvut.cz](mailto:ondrej.svanda@fsv.cvut.cz)*

### ABSTRACT

The aim of the research was to carry out a hydraulic design of rowing/sculling and paddling simulator. Nowadays there are two main approaches in the simulator design. The first one includes a static water with no artificial movement and counts on specially cut oars to provide the same resistance in the water. The second approach, on the other hand uses pumps or similar devices to force the water to circulate but both of the designs share many problems. Such problems are affecting already built facilities and can be summarized as unrealistic feeling, unwanted turbulent flow and bad velocity profile. Therefore, the goal was to design a new rowing simulator that would provide nature-like conditions for the racers and provide an unmatched experience. In order to accomplish this challenge, it was decided to use in-depth numerical modeling to solve the hydraulic problems. The general measures for the design were taken in accordance with space availability of the simulator's housing. The entire research was coordinated with other stages of the construction using BIM. The detailed geometry was designed using a numerical model in Ansys Fluent and parametric auto-optimization tools which led to minimum negative hydraulic phenomena and decreased investment and operational costs due to the decreased hydraulic losses in the system.

### KEYWORDS

Rowing simulator, sculling simulator, paddle simulator, hydraulic research, numerical modeling, building information model, BIM.

### INTRODUCTION

In today's sports world there is a huge competition in every subject no matter if it is athletics, team sports or individual disciplines. Multi-phase everyday practices with carefully chosen nutritious diet and foreign sport camps are the daily routine for the most of the athletes. So it is no surprise that all the teams and coaches are constantly seeking for new ways of improving the athletes' training. As a slightly different method or training device can provide a little advantage that makes the difference in the race.

For rowers and paddlers one of the ways how to increase the technique and to stay in shape during the winter months is to build an indoor rowing/paddling simulator. That allows them to continue the practices even when the weather would not allow it. As a part of a reconstruction project of Labe Arena it was decided, that such a facility should be developed.

Nowadays there are two main approaches in the rowing simulator design. The first uses static water with no artificial movement and counts on specially cut oars to provide the same resistance in the water. This solution lacks the stability when rowing, feels unrealistic, causes undesirable turbulence from the oars and provides bad velocity profile. The second

approach, on the other hand integrates pumps or similar devices to force the water to circulate but all the facilities world-wide share the same drawbacks such as slow water velocity, insufficient water depth and also bad velocity profile. Therefore, the goal was to design a new rowing simulator that would provide nature-like conditions for the racers and avoid all the faults made in the past designs of such facilities.

The contractor for this project was chosen to be the company di5 architekti inženýři s.r.o. For the rowing and paddling simulator it was then decided that it should be designed by CTU in Prague, Faculty of Civil Engineering, Department of Sanitary and Ecological Engineering thanks to a lot of experience with hydraulic research. The aim was to design a facility with circularly pumped water to allow for the rowers and paddlers to experience training conditions that would resemble those in a natural river or channel where the practices usually take place. Some facility parameters are shown in the following Table.

Tab. 1: Facility parameters

	Rowing simulator	Paddling simulator
Construction size	19 x 12.5 m	14.5 x 4 m
Max stream velocity	4 m/s	2.4 m/s
Water depth for sport	0.45 m	0.65 m
Max flow per channel	3.85 m <sup>3</sup> /s	1.33 m <sup>3</sup> /s
Max power req.	150 kW	50 kW

The measurements of the facility were chosen due to the limitations of the housing object and were settled at 19 x 12.5 m of floor plan for both rowing and paddling simulator. In addition, the investor wanted the water velocity to reach up to 4 m/s which significantly overcomes values of any other simulator that has been in operation. The last but not least was the effort to manage and minimize both investment and operational costs of the entire project. The basic shape for the rowing simulator were two rectangular tanks horizontally separated for the water circulation. That was managed with a use of submersible pumps. The area between the tanks was allocated for the seats, rowing equipment and racers themselves. In the original design the paddling simulator was supposed to be a part of the bigger rowing simulator but after first calculations and negotiations with the investor this idea was abandoned and it was decided that the paddling simulator shall be a standalone facility placed next to the rowing one. As a structure material was chosen concrete with smoothed surface and extra epoxide coating to minimal hydraulic losses. Inlet elbow, diffuser, fin and tray were designed to be made of stainless steel. The schematic of the design is shown in Fig. 1.

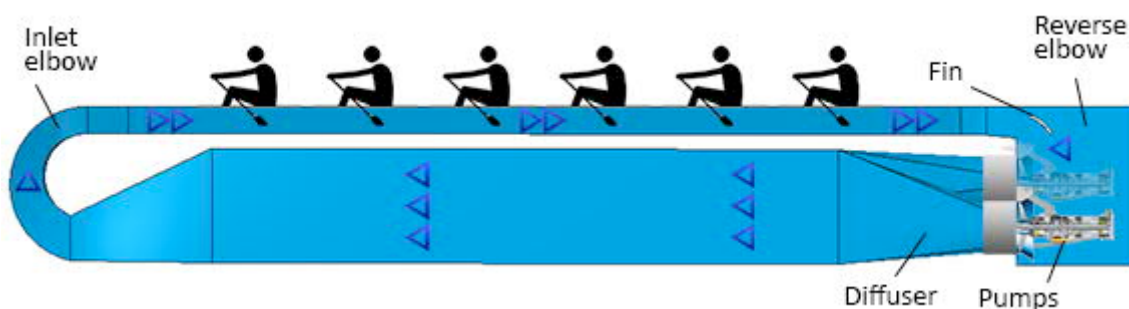


Fig. 1: Rowing simulator design schematic

Given the fact that there is no such a complex facility with similar parameters, it was necessary to come up with an entirely new design. This was achieved using technical calculations and simulations of water flow modeled in both 2D and 3D in Ansys Fluent. The optimization of the geometry was done within parametric tool Direct Optimizer. Some basic model parameters are listed in the following table.

Tab. 1: Basic numerical model parameters

Viscosity model	$\kappa$ - $\epsilon$
Multiphase	Volume of Fluid
Nodes	Ca. 1 000 000

### ROWING SIMULATOR

In the rowing simulator design, it was necessary to calculate the bottom slope first. This value is important in order to secure horizontal water level. Its calculation is based on Bernoulli equation and is calculated from two profiles (inlet and outlet of the rowing platform). The difference between energy in those profiles must match hydraulic losses. The losses were calculated using Chezy equation with Manning velocity coefficient. Result of the iterative process was  $i_0 = 0.0023$ . In terms of absolute height, it means 35 mm of height difference on 15 m of length.

In the next step different flow velocities were evaluated in view of creating waves which is an unwanted phenomenon in the rowing area. The evaluation was done by using Froude number. The magnitude of the Froude number determines the flow regime. The transition from supercritical to subcritical flow is accompanied by hydraulic jump which can cause waves and negative hydraulic phenomena. This transition occurs when the Froude number moves around 1. It is clear from the calculations that the ideal conditions for running the simulator are with the flow from 0 to 2.3 m<sup>3</sup>/s and then from 3 to 4 m<sup>3</sup>/s. Accordingly from 0 to 1.9 m/s and from 2.3 to 3.1 m/s.

### Pumps

Both left and right circuit of the rowing platform are equipped with submersible pumps whose are to provide sufficient flow and velocity. The requirements for these pumps were quite extraordinary, therefore the selection was very narrow. The output power should have been approximately 4 m<sup>3</sup>/s with 1 m of discharge head. Also, the type must be a propeller pump in order to provide uniform velocity field at the outlet which leads to a steady water level in the rowing area. The only pumps to meet these requirements were from Amaline series, specifically 3x S 8032-465/304URG (25 kW) were used for each circuit. The combined power for each circuit was then 75 kW adding to a total of 150 kW for the entire rowing simulator.

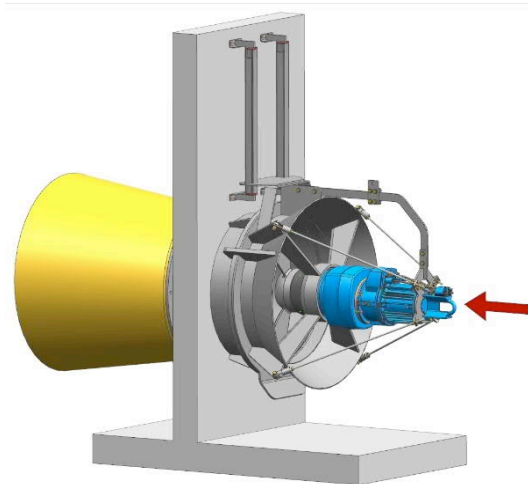


Fig. 2: Proposed propeller pump AMALINE (25 kW)

### Diffuser

Important part of the design is a diffuser. It is located at the pumps discharge which are directly connected to the steel pipe flange with a diameter DN 800 and a length of 0.5 m. The main purpose of the diffuser is to provide as good diffusion of the pumped water as possible so the created velocity profile stays uniform. Besides that, the geometry of the diffuser must also cause low hydraulic losses because of the potential underpressure leading to cavity and possibly damaging the diffuser. The geometry was designed to best diffuse the water from all of the 3 pumps. The length was chosen with low manufacture costs having in mind. The shape and basic measures are shown in the following figure.

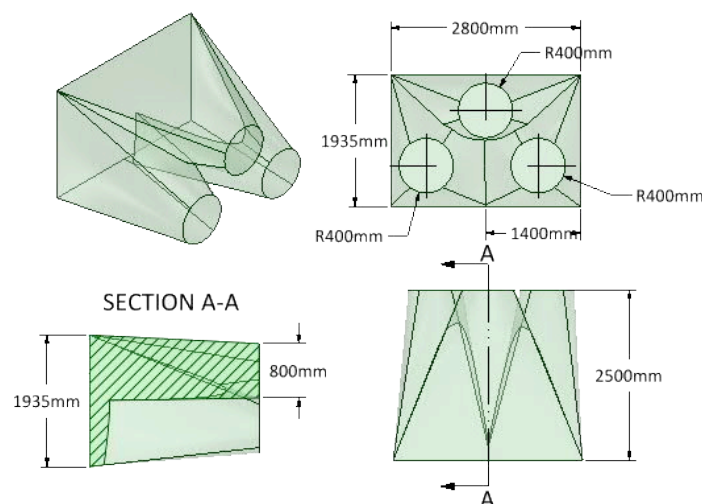


Fig. 3: Geometry of the diffuser

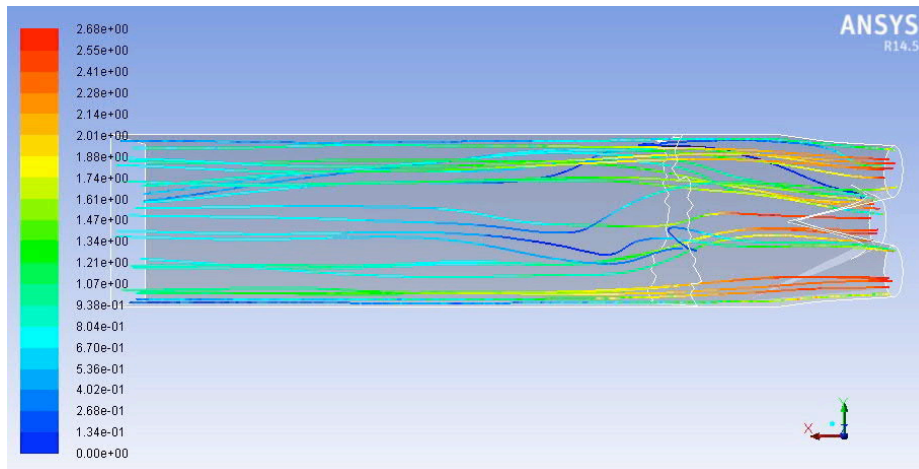


Fig. 4: Pathlines colored by velocity

### Inlet elbow

More than 350 different geometries were simulated in the process of designing the inlet elbow. It was achieved using a 2D model in Direct Optimizer tool. The criteria for the calculation were set to minimum hydraulic losses and uniform outlet velocity field. The optimization started with a choosing of 200 random geometries within a certain range that were subsequently reduced using Kiring method in order to find those where matching the criteria were expected. After choosing 30 potential geometries, the simulation was carried out and the final 5 best geometries were found. The outcome of this process and the optimal geometry for the inlet elbow is shown in the next figure. Appropriate velocity profile can be seen at the end of the inlet elbow (center top).

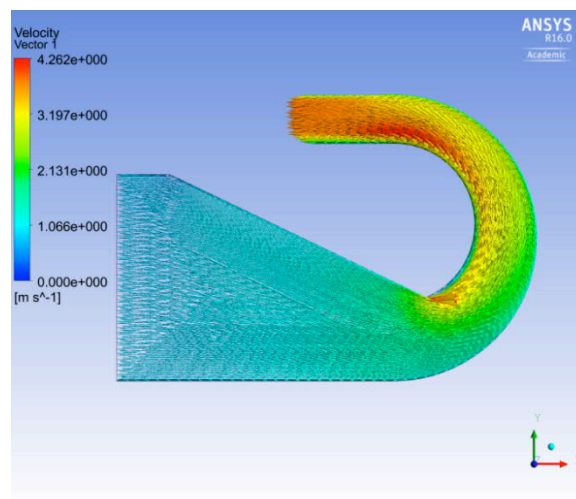


Fig. 5: Velocity vectors shown in the inlet elbow geometry

Obtained velocities and losses were slightly distorted due to the fact that the simulation was run using 2D instead of 3D, therefore the real geometric shape of the construction was not applied. Nevertheless, in this case 2D represents the outcome more than sufficiently and can be used for 3D design. The main reason for choosing 2D was to significantly lower the processing time which led to the ability to compare and evaluate more geometries.

In the next step, the transition from the elbow (pipe flow) to rowing area (open channel flow) was verified for potential wave appearance which would negatively affect the rowing experience. Outcome of the simulation proved the correctness of the design. The water flows into the rowing area with uniform velocities and does not tend to create waves of other unwanted phenomena. In the following picture you can see the phase boundary between water and air in the open channel.

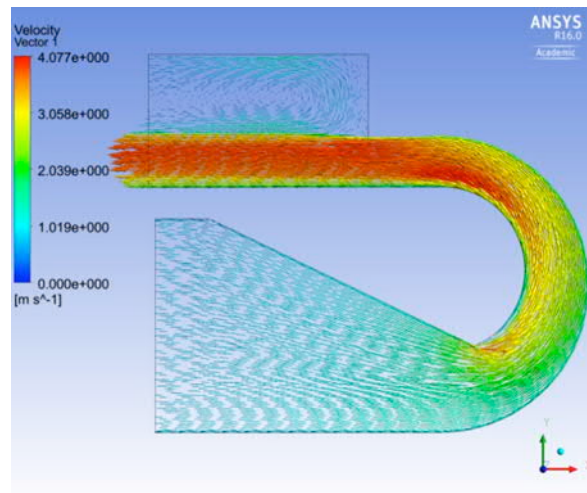


Fig. 6: Velocity vectors at the phase boundary

### Reverse elbow

The geometry of reverse elbow is determined by the space availability due to the pumps' specifications and installation requirements. The inlet parameters were improved by implementing a fin. The optimal design of the fin was found out by testing 10 different geometries with choosing the best one in the end. It turned out that the best solution would be a 1-fin variant because of its low losses. By adding more fins in the design there was no improvement achieved in means of flow parameters and uniformity of the velocity field. In addition, the design of the fin prevents air intake by the pumps. It is designed to fulfill its function the best when the flow reaches the maximum at  $3.85 \text{ m}^3/\text{s}$ . It must be taken in mind that it may not function optimally with lower flows.

The fin is designed in a way that it can be detached in order to allow the installation of the pumps and for their better maintenance. In the proximity of the reverse elbow there is a whitewater area. A special attention was paid to this area to make sure that the whitewater does not occur in the rowing area but remains close to the reverse elbow and the pumps. The outcome of this evaluation is a design modification where the trapezoid stainless steel sheet is extended to the reverse elbow area and is ended with a sharp edge. In the next figure you can see the geometry of the reverse elbow including the fin.

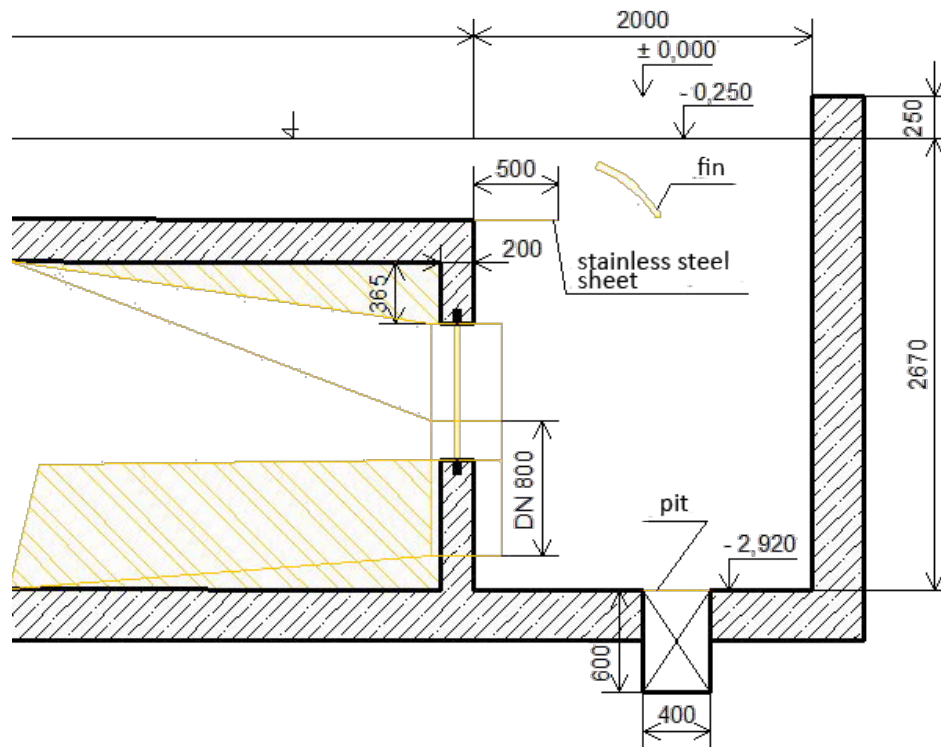


Fig. 7: Geometry of the reverse elbow with the fin

### Flow simulation

Simulation of the flow in the whole rowing simulator was carried out in Ansys Fluent software using 3D model which describes the flow in the simulator the best. During the simulation the velocity of the flow was gradually increased in order to simulate the start of the pumps. It turned out that the design causes waves in the rowing area. After a geometry modification in the rowing area the following simulation proved to provide a steady flow at  $3.85 \text{ m}^3/\text{s}$  in each channel. At this setting the water level is steady with no waves and uniform velocity profile. The turbulence occurs behind the rowing area in the reverse elbow which is perfectly acceptable. The flow simulation with highlighted water level can be seen in the following figure.

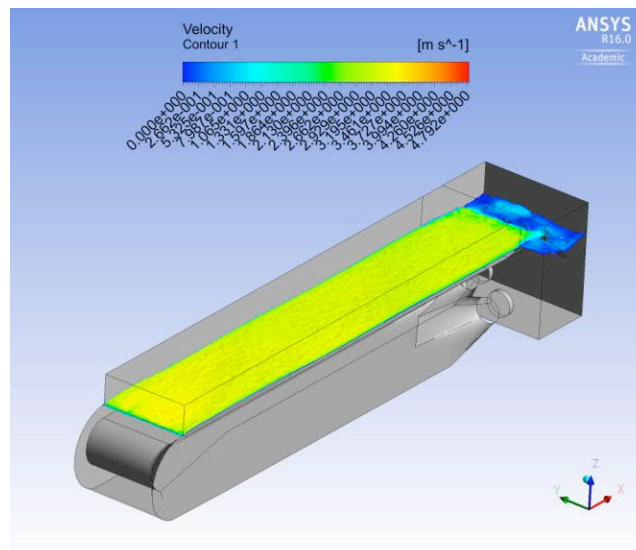
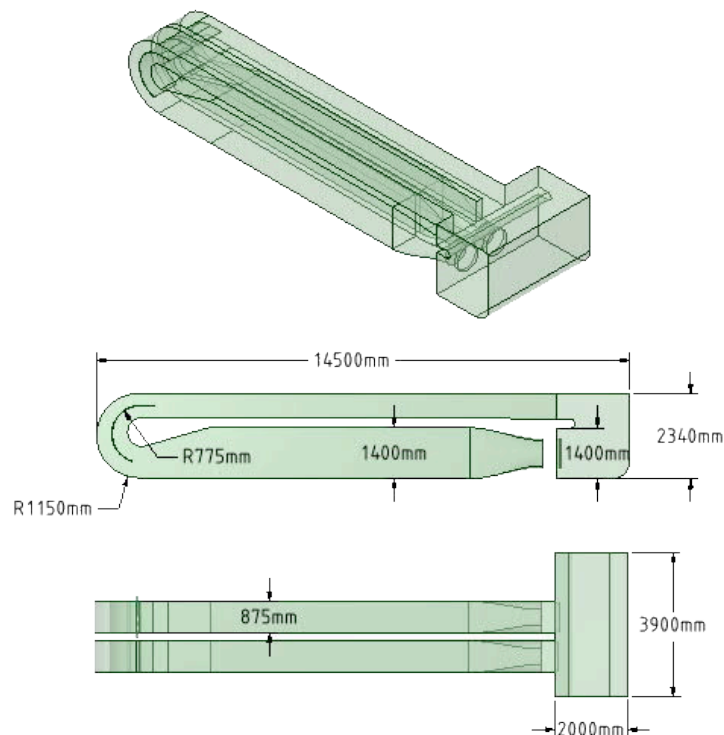


Fig. 8: Flow simulation with highlighted water level

### PADDLING SIMULATOR

The design of the smaller paddling simulator was carried out in the same way as the bigger rowing one. The bottom slope was calculated including the magnitude of the horizontal force caused by the dynamics of the flow. Also different flow velocities were simulated for the wave occurring. Subsequently all the optimal geometries of the diffuser and both elbows were found using numerical model and Ansys Fluent program with the help of Direct Optimizer tool. The aim of the design were low hydraulic losses, steady flow and water level. Pumps were chosen to be the same AMALINE as in the rowing simulator. In this case only 1 pump is needed for each channel, totalling in 2 pumps of a 50 kW outcome power. Finally, the entire paddling simulator was evaluated in 3D to make sure all the designed parts make a perfect whole and no unwanted hydraulic phenomena occur in the design. The final design of the paddling simulator is shown in Fig. 9.



*Fig. 9: Final design of the paddling simulator*

## CONCLUSION

A new design in the area of the rowing and paddling simulators was created with suitable geometry and hydraulic conditions. The new approach lies in the use of 2D and 3D numerical model and its evaluation in the Ansys Fluent software. In addition, a parametric tool Direct Optimizer was used to find the best suitable geometry for chosen conditions. The aim was to design a facility that would provide steady water level with high velocities, low hydraulic losses, uniform velocity field in the rowing and paddling area and low investment and operation costs. Also the dynamic forces of the construction were calculated with a respect to the structure of the housing.

The initial goal of creating a new generation of rowing and paddling simulator with significantly better training conditions and low operational costs was met. After the last simulation it is clear that despite the high velocity in the rowing simulator, the water level stays steady with no waves occurring in the rowing area. With additional funds from the investor, it is plausible that the development of the simulator could be improved in a way of adding a device that would follow the rowing movement dynamics.

## ACKNOWLEDGEMENTS

This work was supported by Technological agency of the Czech Republic: TAČR TE02000077 Smart Regions – Buildings and Settlements Information Modelling, Technology and Infrastructure for Sustainable Development and by the Student Grant Foundation of CTU: SGS16/205/OHK1/3T/11.

Access to computing and storage facilities owned by parties and projects contributing to the

National Grid Infrastructure MetaCentrum, provided under the program "Projects of Large Infrastructure for Research, Development, and Innovations" (LM2010005), is greatly appreciated.

## REFERENCES

1. Streeter, V.L., Wylie, E.B. and Bedford, K.W. *Fluid Dynamics. Ninth Edition.* s.l. : Mc Graw-Hill Book Company, Inc, 1998. ISBN 0 07 062537 9.
2. Streeter, V.L., Wylie, E.B. and Bedford, K.W.. *Handbook of Fluid Dynamics. First edition.* s.l. : Mc Graw-Hill Book Company, Inc., 1961. ISBN 978-0070621787.